The Planetary Science Journal, 3:243 (21pp), 2022 October https://doi.org/10.3847/PSJ/ac8ced
© 2022. The Author(s). Published by the American Astronomical Society.
OPEN ACCESS

3 μm Spectroscopic Survey of Near-Earth Asteroids

L. E. McGraw[1], J. P. Emery[1], C. A. Thomas[1], A. R. Rivkin[2], N. R. Wigton[3], and M. McAdam[4]
[1] Northern Arizona University, Department of Astronomy and Planetary Science, P.O. Box 6010, Flagstaff, AZ 86011, USA; lem366@nau.edu
[2] JHU/APL, 211100 Johns Hopkins Road, Laurel, MD 20723, USA
[3] Oak Ridge National Laboratory, 1 Bethel Valley Road, Oak Ridge, TN 37831, USA
[4] SOFIA Science Center, NASA Ames Research Center, Mail Stop N232-12, P.O. Box 1, Moffett Field, CA 94035, USA
Received 2022 April 6; revised 2022 July 7; accepted 2022 July 7; published 2022 October 27

Abstract

Near-Earth Asteroids (NEAs) are excellent laboratories for processes that affect airless body surfaces. S-complex (including V-type) NEAs were not expected to contain OH/H_2O on their surfaces because they formed in the anhydrous regions of the solar system and their surface temperatures are high enough to remove these volatiles. However, a 3 μm feature typically indicative of OH/H_2O was identified on other seemingly dry bodies in the inner solar system, raising the question of how widespread volatiles may be on NEAs. We observed 29 NEAs using both prism (0.7–2.52 μm) and LXD_short (1.67–4.2 μm) modes on SpeX on NASA's IRTF in order to accurately characterize asteroid spectral type and the 3 μm region. Eight of the observed NEAs have a 3 μm absorption feature at $>1\sigma$ (three of which are present to $>2\sigma$), and they exhibit four identified band shape types. Possible sources for OH/H_2O on these bodies include carbonaceous chondrite impacts and/or interactions with protons implanted by solar wind. Characteristics such as composition and aphelion appear to play an important role in the delivery and/or retention of OH/H_2O, as all eight NEAs with an absorption feature are S-complex asteroids and six enter the main asteroid belt. Additionally, perihelion, size, albedo, and orbital period may play a minor role. Our observations determined that nominally anhydrous, inner solar system bodies, and therefore near-Earth space in general, contain more OH/H_2O than previously expected. The identified trends should help predict which NEAs that have not yet been observed might contain OH/H_2O on their surfaces.

Unified Astronomy Thesaurus concepts: Near-Earth objects (1092); Spectroscopy (1558); Near infrared astronomy (1093); Asteroids (72); Surveys (1671); Ground-based astronomy (686)

Supporting material: data behind figure, figure set

1. Introduction

Volatiles such as hydroxide and water (OH/H_2O) are considered necessary components for any habitable world (e.g., Morbidelli et al. 2000). Looking for these materials on planetary bodies can aid in assessing their past and future habitability, in addition to determining the OH/H_2O budget of various regions of space. In particular, characterizing OH/H_2O on near-Earth asteroids (NEAs) can aid in explaining how water was delivered to Earth even though it formed within the frost line (Lunine 2006). Most airless bodies that formed (or accreted) in the inner solar system, that is, interior of the 3:1 Jupiter resonance in the main asteroid belt (2.5 au), are generally considered to be nominally anhydrous because nebular temperatures and pressures precluded the formation and condensation of volatile-rich materials (e.g., Grossman & Larimer 1974) and the lack of atmospheres precludes the stability of secondary OH/H_2O on their ordinary-chondrite-like surfaces (e.g., Muralidharan et al. 2008). In particular, these bodies formed within the frost line in the solar system, so water and hydroxide typically could not condense.

Recent studies have detected OH/H_2O on nominally anhydrous, inner solar system surfaces using 3 μm spectroscopy, one spectral region in which O–H bonds absorb light. Sunshine et al. (2009), Pieters et al. (2009), and Clark (2009), using data from the Deep Impact, Chandrayaan-1, and Cassini missions, respectively, discovered a shallow but clear 3 μm absorption feature on the Moon that was present at all latitudes (see Figure 1(c) from Sunshine et al. 2009). More recent work (e.g., Simon et al. 2019; Ruiz et al. 2020; Honniball et al. 2021) has both confirmed and studied the lunar absorption feature in more detail. In 2012, De Sanctis et al. (2012) used data from the Dawn mission to show that Vesta, the largest asteroid in the main belt ($a = 2.36$ au) also exhibits a 3 μm feature and therefore contains water and/or hydroxide on its surface (see Figure 2(c) in De Sanctis et al. 2012). Both Vesta and the Moon are inner solar system airless bodies, suggesting that bodies in this region of space support surface volatiles, despite their presumably anhydrous formation. Most NEAs formed in roughly the same environment as Vesta and occupy roughly the same environment as the Moon, so should therefore also contain OH/H_2O on their surfaces. Data from Rivkin et al. (2018) support this hypothesis, with near-infrared (NIR) spectra showing a 3 μm feature on the two largest NEAs, (1036) Ganymed and (433) Eros, both of which are S-type asteroids and were previously believed to be anhydrous. Identifying the distribution of OH/H_2O within the NEA population will constrain the OH/H_2O budget of the inner solar system, as well as aid in general compositional understanding of this varied population. Such a study aids in not only understanding solar system formation but also hazard mitigation for spacecraft and planetary defense (e.g., Lee 1996; Britt et al. 2002; Opeil et al. 2012; Perna et al. 2013), as well as asteroid resource utilization (e.g., Lewis & Huston 1993; Nichols 1993; Sanchez & McInnes 2012).

Original content from this work may be used under the terms of the Creative Commons Attribution 4.0 licence. Any further distribution of this work must maintain attribution to the author(s) and the title of the work, journal citation and DOI.

2. Background

2.1. H_2O and OH on Asteroid Surfaces

Molecular water (H_2O) and/or hydroxide (OH) can be identified on an asteroid by conducting NIR reflectance spectroscopy. Specifically, the bond between an oxygen atom and a hydrogen atom has a fundamental vibrational frequency equivalent to a wavelength between ∼2.5 and 3 μm (e.g., Benedict & Plyler 1951). The band can extend up to ∼3.5 μm, and the exact band center and shape are dependent on the composition and phase of the molecule containing the bonded hydrogen and oxygen (e.g., Rivkin et al. 2002). Band depth is also diagnostic of the nature of the OH/H_2O present, as a deep absorption feature is generally indicative of OH/H_2O contained in the mineral structure, whereas a shallow feature indicates that the molecules are isolated and present in a smaller quantity (e.g., Pieters et al. 2009).

The 2–4 μm region can be difficult to study using ground-based telescopes, as atmospheric water vapor absorbs almost 100% of the radiation between approximately 2.55 and 2.85 μm. Despite such difficulties, 3 μm spectroscopy is the best ground-based observing method for remotely determining the presence of OH/H_2O on asteroid surfaces because the long-wavelength edge of the absorption band is still detectable.

2.2. Delivery Mechanisms

Four potential sources for OH/H_2O on airless bodies have been previously suggested: native phyllosilicates (e.g., Brearley & Jones 1998), exogeneous carbonaceous material (McCord et al. 2012; De Sanctis et al. 2012), exogeneous/indigenous cometary material (e.g., Greenwood et al. 2011; Neumann et al. 2013; Bottke et al. 2002; DeMeo & Binzel 2008), and solar wind proton implantation (e.g., Zellner et al. 1966; Starukhina 2001; Pieters et al. 2009; Sunshine et al. 2009; Clark 2009). Phyllosilicates compose approximately 21%–30% of the main belt by mass based on analyses of carbonaceous chondrite meteorites (Brearley & Jones 1998). The main belt is ∼35%–50% C-complex material by mass, though only ∼60% of such asteroids contain OH/H_2O (DeMeo & Carry 2013). Other taxonomic classes, primarily M types, also exhibit a relatively deep ($\gtrsim$10%), linearly increasing feature with peak absorption centered around 2.7 μm 3 μm feature that is suggestive of phyllosilicate-bound hydroxide (Rivkin et al. 1995, 2000; Landsman et al. 2015; Takir et al. 2017). The mass of phyllosilicates in the NEA population is less constrained owing to limited observations in the 2–4 μm region. As NEAs are not uniformly sampled from the main belt, they are not a representative population of main belt asteroids (MBAs). Only ∼15% are expected to contain phyllosilicates (Binzel et al. 2019), and some NEAs experience high enough temperatures to dehydrate surface phyllosilicates (Marchi et al. 2009), making the actual quantity of phyllosilicates in near-Earth space uncertain. Most NEAs belong to the S-complex (Binzel et al. 2015), which are not expected to contain phyllosilicates.

Carbonaceous and cometary impacts are potential exogenous sources of OH/H_2O on NEAs. Comets are thought to have delivered water to the Moon and Mercury (e.g., Greenwood et al. 2011; Neumann et al. 2013) and so are a potential source on NEAs as well. Additionally, a small percentage (∼6%–8%) of NEAs are likely of cometary origin (Bottke et al. 2002; DeMeo & Binzel 2008). Absorption features related to comets would be more bowl-like, rather than sharp or linear, due to H_2O being the predominant species over OH (e.g., Rivkin & Emery 2010; Takir & Emery 2012). The Dawn mission revealed numerous impact craters surrounded by low-albedo, hydrated material on the surface of the MBA Vesta (e.g., Prettyman et al. 2012; McCord et al. 2012; Reddy et al. 2012a). Vesta's 3 μm features are strongly spatially correlated with these dark craters, suggesting that hydrated carbonaceous material composed the impactors (McCord et al. 2012; De Sanctis et al. 2012). It is expected that water and/or hydroxide delivered via this mechanism would be correlated with craters on other bodies as well. The features associated with exogeneous carbonaceous material vary in shape: one type has an absorption peak at 2.81 μm, and one is very wide with a hard-to-define long-wavelength limit (De Sanctis et al. 2013). Some features appear similar in shape to those of native phyllosilicates, though shallower and with a rounded absorption peak (De Sanctis et al. 2012), while the disk-integrated feature appears as a shallow, zero-sloped feature that steeply increases to the reflected continuum at the long-wavelength end of the band (see Section 6.4). Carbonaceous and cometary materials are more common in the outer main belt and beyond than in the inner solar system (e.g., DeMeo & Carry 2013), and carbonaceous/cometary impacts may therefore be expected to be more likely only for NEAs with orbits that take them into the outer main belt (i.e., large aphelia).

Solar wind proton implantation offers another method of exogenous OH/H_2O delivery. Features caused by this mechanism most closely resemble that of native phyllosilicates, but much shallower (e.g., Sunshine et al. 2009). The solar wind is primarily composed of hydrogen ions, and it flows outward from the Sun in all directions at speeds around 400 km s^{-1} (Smith 1967). These ions then bombard any surface impacted by the solar wind, which is any surface visible to the Sun that is not protected by a magnetic field or thick atmosphere. OH/H_2O implantation via proton bombardment is a multistep process. A surface is first mechanically weathered by solar radiation, micrometeorites, or the solar wind, creating crystalline defects and dangling bonds. The vacancies then trap solar wind protons, and if the diffusion time is sufficiently large, the hydrogen ions form bonds with any free oxygen ions to create OH and possibly H_2O that is not necessarily bound to other molecules (Starukhina 2001, 2003, 2006; Farrell et al. 2015, 2017). Recent laboratory studies, however, suggest that solar wind proton implantation alone is not sufficient to create H_2O, or potentially even OH, without some additional process, such as recombinative desorption or micrometeorite impacts (Burke et al. 2011; Schaible & Baragiola 2014; Orlando et al. 2018; Zhu et al. 2019). Nevertheless, this delivery mechanism is still the most likely responsible for any shallow 3 μm absorption features on NEAs and is potentially responsible for the 3 μm signature observed on the Moon, as apparent diurnal variations in the band depth correlate with solar orientation (Sunshine et al. 2009). However, recent work (e.g., Ruiz et al. 2020) suggests that the aforementioned diurnal variations are artifacts of inexact thermal tail removal, and properly accounting for various conditions such as surface roughness removes the diurnal variations previously noted. Research into the exact composition, distribution, and delivery of lunar OH/H_2O is ongoing (e.g., Honniball et al. 2021). Through the disk-integrated NIR spectroscopic survey of NEAs presented

herein, we constrain the variables that control delivery and retention of OH/H_2O to NEA surfaces.

3. Methods

3.1. Data Acquisition

Spectra were collected using the SpeX instrument on NASA's Infrared Telescope Facility (IRTF) on Maunakea, Hawaii (Rayner et al. 2003). A shallow 3 μm absorption feature, indicative of the presence of O–H bonds, typically has a depth of only a few percent, so we targeted a signal-to-noise ratio (S/N) of ~50. The SpeX instrument can achieve the required S/N for asteroids with $V < 14$ mag with 2–3 hr of integration time. We attempted to observe all NEAs that surpassed this brightness requirement, regardless of spectral type and therefore native composition, since the start of this project in 2016 through 2020, as well as several targets from an earlier preliminary study (Table 1), but several objects were not observed owing to weather or technical issues. We also observed two MBAs to compare to (1036) Ganymed, one of the NEAs studied. We report here spectra of 29 NEAs and 2 MBAs.

We used two gratings to fulfill the requirements of this study, both with a $0.8'' \times 15''$ slit. The long-wavelength cross-dispersed short mode (LXD_short), which spans 1.67–4.2 μm, captures the 3 μm OH/H_2O feature, whereas the prism mode (0.7–2.5 μm) enables spectral type and mineralogical determinations. We also used the Guidedog (K band) and MIT Optical Rapid Imaging System (MORIS; V band) cameras to track the targets and collect NIR and visible images for future analysis. The observing procedure used requires the telescope to alternate between the NEA and selected local standard star every 10–30 minutes to ensure that the background noise and absorption features due to telluric water can be adequately removed. The telescope nodded between two positions within the slit when observing both the standard star and target NEA to enable the subtraction of background sky emission.

3.2. Data Processing

The data were downloaded from the IRTF servers and processed using a variety of IDL-based software tools. The Spextool package (Cushing et al. 2004; Vacca et al. 2003) was used to flat-field correct, extract, and wavelength-calibrate spectra from the raw data collected by the telescope. For the LXD spectra, atmospheric absorptions were removed by dividing the extracted NEA frames by the extracted analog star frames observed at similar air mass. A subpixel shift was computed and applied before division to assure that the NEA and star frames were properly aligned. For the prism spectra, a grid of ATRAN-derived model atmospheric transmission curves was used to remove the atmospheric absorptions by determining the best-fit transmission model to our data, i.e., varying the water vapor content to match the absorption depth in each NEA and star frame (MacLennan 2019). Subpixel shifting and division by the analog star were performed as for the LXD spectra. After division by the star, the spectral frames were combined into a single spectrum. During this step, the individual spectra were scaled to each other before being combined using the standard error robust mean statistical method. Finally, the seven orders of the LXD_short combined spectrum were merged into one continuous spectrum. The Spextool merging code allows the orders to be scaled to each other and lower-S/N data at the edges of each order (at wavelengths where contiguous orders overlap) to be trimmed prior to merging (Cushing et al. 2004).

3.3. Thermal Tail Removal

The longer-wavelength portion of the LXD spectrum ($\lambda \gtrsim 2.8\ \mu$m, depending on surface temperature) contains a significant thermal component. The thermal tail is removed, after normalization, using a thermal model based on the near-Earth asteroid thermal model (NEATM; Harris 1998). This model, like the standard thermal model (STM), uses the subsolar temperature ($T_{SS} = \left(\frac{(1-A)*L_0}{4\varepsilon\sigma\eta\pi R^2}\right)^{0.25}$) to calculate thermal flux (Lebofsky & Spencer 1989; Harris 1998). The reflected continuum from shorter wavelengths is extrapolated to approximate the linear spectrum at longer wavelengths. The continuum slope and vertical position, along with the beaming parameter in the NEATM, are varied to produce the best-fit continuum, which results in the spectrum at $\lambda > 3.3\ \mu$m lying along the continuum (Figure 1). The band depth, defined as the difference between the continuum and the reflectance at 2.9 μm, is calculated to determine whether the NEA contains OH/H_2O on its surface. The error in band depth includes propagation of uncertainties from the spectrum and the point-to-point spread in the data. Additionally, RELAB spectra (1.6–4.05 μm) of ordinary chondrite powders were analyzed to verify that continuum slopes selected in this work were reasonable based on meteorite spectra and to determine an expected standard deviation in continuum slope. While space weathering is expected to increase the spectral slopes of asteroids relative to generally fresh meteorite spectra (e.g., Hapke 2001), the average 2 μm spectral slope of our targets is within 1σ of the average 2 μm spectral slope of the RELAB spectra used in this study. The band depth was recalculated with the $\pm 1\sigma$ continuum for those NEAs with an identified 3 μm feature, and the differences in band depth between the positive and negative 1σ slopes and the best-fit slope were added in quadrature to the previously calculated uncertainty. For those NEAs without an identifiable 3 μm feature, the average of this additional uncertainty (0.8%) was added in quadrature to the previously calculated error to account for error in selecting an appropriate continuum.

3.4. Band Parameter Analysis

3.4.1. Prism Bands

For S-complex and V-type asteroids, the 1 μm and 2 μm absorption bands in the spectra (BI and BII, respectively) were characterized by the band center wavelengths (BIC and BIIC) and the band-area ratio (BAR). This band parameter analysis was conducted on the prism data using the Band Analysis Routine for Asteroids (BAR-Ast; MacLennan 2019), an algorithm based on the Spectral Analysis Routine for Asteroids (SARA; Lindsay et al. 2015). SARA uses fifth-order polynomials to define the wavelength minima and maxima of BI and BII, after which it fits third-, fourth-, and fifth-order polynomials to BI and BII to find the band centers and other band parameters. The BAR-Ast algorithm does not assume a polynomial fit to the band, instead using a nonparametric smoothing algorithm, producing more accurate results (Figure 2; see also Figure 3.4 from MacLennan 2019). The uncertainty of each band parameter is computed using a Monte

Table 1
Observing Parameters and Conditions of NEAs (MBAs at Bottom)

Object		Date (UT)	V mag[a]	LXD Mid-time (UT)	LXD Int. Time (s) × Images	Prism Mid-time (UT)	Prism Int. Time (s) × Images	Standard Star	Solar Dist. (au)	Earth Dist. (au)	Phase Angle	Weather[b] (Seeing)
433	Eros	4-Jan-2019	8.3	9:03	30 × 128	6:12	3 × 8	HD 28005	1.153	0.214	34.06	Cl (0.5″)
1036	Ganymed	19-Oct-2011	8.3	10:04	20 × 240	7:50	1 × 16	HD 12846	1.349	0.365	12.82	Ci (0.4″)
1627	Ivar	15-Jun-2018	11.9	9:20	30 × 144	6:39	30 × 16	HD 129290	1.245	0.352	42.99	Cl (0.6″)
1685	Toro	27-Jan-2016	13.1	6:40	20 × 160	8:28	60 × 2	SAO 130276	1.008	0.163	77.15	Cl (0.7″)
1981	Midas	19-Mar-2018	12.4	8:28	30 × 160	5:51	60 × 16	HD 70516	1.042	0.098	59.58	Cl (0.5″)
3122	Florence	4-Sep-2017	9.5	8:58	30 × 116	6:32	8 × 8	HD 197076	1.044	0.052	45.90	Cl (0.6″)
3200	Phaethon	15-Dec-2017	10.4	7:25	30 × 32	…	…	HD 12074	1.038	0.075	42.82	Cl, VW (1.8″)
5143	Heracles	13-Nov-2016	13.3	13:40	30 × 160	10:45	60 × 10	HD 40848	1.177	0.283	43.16	Cl (0.8″)
6063	Jason	7-Jun-2017	14.1	8:05	30 × 80	6:35	120 × 16	HD 135724	1.148	0.183	39.69	PC (0.8″)
25916	2001 CP44	21-Jun-2018	13.0	10:30	30 × 64	…	…	HD 148729	1.347	0.353	17.60	Cl (0.6″)
54789	2001 MZ7	1-Feb-2010	13.6	12:14	15 × 60	11:02	120 × 8	SAO 97431	1.284	0.305	9.90	Ci (0.6″)
66146	1998 TU3	4-Oct-2017	13.1	14:00	30 × 128	11:18	120 × 4	HD 25710	1.150	0.214	41.46	F (0.6″)
66391	Moshup	26-May-2019	12.6	…	…	5:36	50 × 8	HD 75023	1.009	0.035	82.88	Cl, W (0.7″)
		29-May-2019	13.0	6:25	30 × 80	…	…	HD 94722	1.024	0.054	76.92	Cl, H (1.0″)
		31-May-2019	13.6	6:15	30 × 86	…	…	HD 101165	1.033	0.074	72.87	Cl (0.5″)
68950	2002 QF15	25-May-2019	14.2	7:22	30 × 154	…	…	HD 96780	1.032	0.101	76.05	Cl (0.7″)
		26-May-2019	14.2	7:43	30 × 126	9:50	60 × 8	HD 98248	1.038	0.107	73.37	Cl, W (0.7″)
85275	1994 LY	7-Aug-2020	14.1	9:42	30 × 128	…	…	HD 163099	1.116	0.158	46.57	F, PaC (0.7″)
96590	1998 XB	27-Nov-2016	13.4	10:49	30 × 116	8:38	30x2;120x4	HD 23925	1.116	0.144	24.01	PC (0.9″)
143404	2003 BD44	2-Apr-2017	14.0	8:30	30 × 128	6:17	120 × 4	HD 99252	1.136	0.146	20.11	Cl (1.2″)
144332	2004 DV24	16-Sep-2018	13.1	7:21	30 × 128	9:17	60 × 8	HD 164509	1.013	0.056	80.72	Cl (1.1″)
153201	2000 WO107	2-Dec-2020	13.4	9:41	30 × 192	12:19	70 × 20	HD 283604	1.040	0.054	2.84	W (0.4″)
159402	1999 AP10	8-Oct-2020	12.6	8:25	30 × 128	10:02	20 × 12	SAO 107923	1.078	0.097	34.39	Cl (1.2″)
		9-Oct-2020	12.6	8:56	30 × 152	…	…	SAO 107932	1.074	0.095	35.96	Cl (0.7″)
163373	2002 PZ39	12-Feb-2020	14.3	8:05	60 × 122	10:31	30 × 8	HD 245025	1.014	0.047	53.70	M Cl (-0.7″)
163696	2003 EB50	24-Nov-2017	13.2	14:07	30 × 116	11:29	120 × 8	HD 268408	1.064	0.101	39.40	Cl (0.7″)
164121	2003 YT1[c]	30-Oct-2016	15.1	…	…	10:58	10 × 40	HD 36387	1.087	0.210	59.53	MC
194126	2001 SG276	25-Apr-2018	13.0	11:22	30 × 128	8:44	90 × 8	HD 127600	1.091	0.085	3.55	Cl (0.7″)
214088	2004 JN13	30-Nov-2014	13.0	11:11	20 × 280	13:48	60 × 2	HD 34239	1.137	0.174	27.32	Cl
285944	2001 RZ11	20-Aug-2014	13.0	10:17	20 × 160	12:21	120 × 4	HD 194764	1.106	0.104	25.12	Cl, dry
332446	2008 AF4	10-Jan-2021	14.3	14:10	30 × 198	11:23	70 × 16	HD 101026	1.003	0.034	54.79	Cl (1.1″)
357439	2004 BL86	27-Jan-2015	10.3	12:03	20 × 280	…	…	HD 76332/76765	0.995	0.011	12.67	Cl
454177	2013 GJ35	8-Jan-2019	13.8	14:02	30 × 160	16:02	90 × 8	HD 76446	1.176	0.209	21.11	Cl (0.6″)
		14-Jan-2019	13.7	11:26	30 × 176	14:14	90 × 8	HD 71710	1.153	0.193	26.24	Cl(0.4″)
	2014 JO25	22-Apr-2017	12.8	8:30	30 × 128	5:43	120 × 4	HD106680	1.056	0.055	23.90	PC (0.8″)
4	Vesta	2-Apr-2017	7.8	5:42	30 × 8	…	…	HD 60298	2.447	2.071	23.73	Cl (1.2″)
349	Dembowska	10-May-2019	11.3	7:18	30 × 128	9:41	40 × 24	SAO 99090	3.153	2.751	18.08	Cl (0.9″)

Notes.
[a] V mag values from JPL Horizons.
[b] (M)Cl—(mostly) clear; Ci—cirrus; PC—partly cloudy; MC—mostly cloudy; PaC—patchy clouds; (V)W—(very) windy; F—foggy; H—humid.
[c] No LXD data for 2003 YT1 owing to poor weather; it is only listed in Tables 1 and 4.

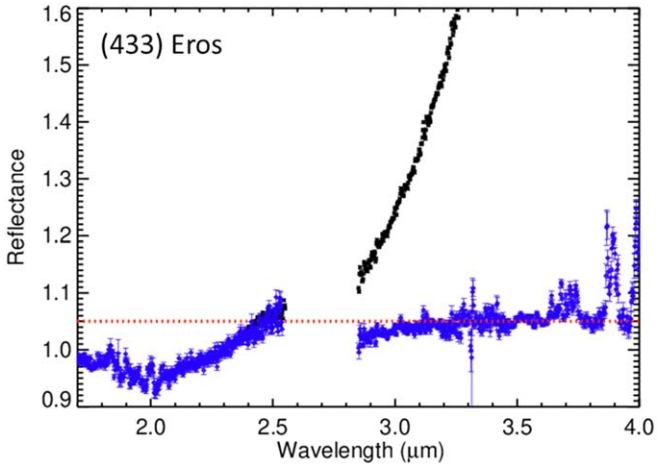

Figure 1. Spectrum (normalized reflectance values vs. wavelength in μm) of (433) Eros as observed on 2019 January 4. Black data points represent the spectrum before thermal tail removal (i.e., reflected and thermal components), blue represents the spectrum after thermal tail removal (i.e., only reflected component), and the red dashed line represents reflected continuum. Data points from 1.7 to 2.55 μm are from prism due to noise in the LXD data.

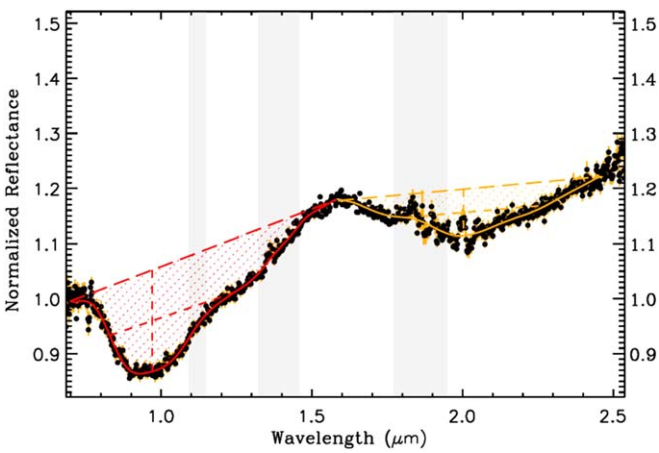

Figure 2. Prism spectrum of (433) Eros observed on 2019 January 4 showing graphical results of BAR-Ast. The red and yellow shaded regions represent band area. The vertical red and yellow dashed lines mark the band centers, and the slanted red and yellow dashed lines mark the continuum and the FWHM of the bands (MacLennan 2019). The gray shaded bars illustrate spectral regions of telluric water vapor absorptions, which were corrected using ATRAN, as described in Section 3.2.

Carlo simulation, in which reflectance values are randomly sampled from a normal distribution based on the 1σ errors at each wavelength. This study used 10,000 iterations for each NEA to compute the parameters and their 1σ errors.

The relations between band parameters and mineralogy were derived using laboratory spectra of meteorite samples, so several corrections are required to properly use the equations for asteroid spectra. Temperature is the main factor to address, as the average room temperature on Earth can differ significantly from the temperature of an asteroid's surface. Sanchez et al. (2012) determined that BII is the most susceptible to temperature differences, so both BIIC and the BAR must be corrected. V-type asteroids require two sets of temperature corrections based on composition. Reddy et al. (2012b) found that both BIC and BIIC are affected by temperature differences, but the exact correction depends on whether the asteroid is more similar to a diogenite or a howardite/eucrite. These corrections, as well as the band parameter equations mentioned above, are summarized in Reddy et al. (2015a). The surface temperature of each asteroid is calculated using the globally averaged equilibrium temperature equation $T_{\rm eq} = \left(\frac{(1-A)*L_0}{16\varepsilon\sigma_{\rm B}\eta\pi R^2}\right)^{0.25}$, where A is the bond albedo, L_0 is the solar luminosity, ε is the emissivity, $\sigma_{\rm B}$ is the Stefan-Boltzmann constant, η is the beaming parameter, and R is the heliocentric distance in meters (Burbine et al. 2009). The beaming parameter used in this study was derived from the thermal model described in Section 3.3.

Correcting for red-edge differences, that is, variations in the maximum wavelength for which reflectance values were collected, is an additional necessary correction between the asteroid and meteorite equations. The BAR-Ast code sets the red edge at 2.45 μm, while the red edge of the meteorite spectra used by Dunn et al. (2010) was 2.50 μm. This difference affects the shape of BII and therefore the BAR. Lindsay et al. (2016) determined two new equations for the BAR: one assumes that the red edge is 2.45 μm, and the other allows for other red edges, though the exact formula depends on which type of ordinary chondrite to which the asteroid is most similar (LL, L, or H). Subsequent work by Sanchez et al. (2020) investigated the dependence of the blue edge (i.e., the short-wavelength limit) of BI on BAR and BIC. Additionally, Sanchez et al. (2020) reduced the S/N of laboratory meteorite spectra to match that of typical asteroid spectra and produced a new set of mineralogical equations taking lower S/N, as well as BI blue edge and BII red edge, into account. Differences in band parameters due to phase angle have also been studied, but they do not have a significant impact on mineralogical determinations (Sanchez et al. 2012; Reddy et al. 2012b).

After applying the corrections, the BIC, BIIC, and BAR are then used to make mineralogical interpretations of the silicate asteroids observed (e.g., Gaffey et al. 1993). For ordinary chondrites, the BAR is a proxy for the relative olivine versus pyroxene content (olivine/[olivine + pyroxene]) and BIC is controlled by the fayalite (Fa) and ferrosillite (Fs) content. The BAR does not provide any mineralogical information for V-type asteroids, but both BIC and BIIC can be used to estimate Fs and wollastonite (Wo) content, as well as the magnesium number, which is the ratio of magnesium to the total magnesium and ferrous iron content of a substance. The equations relating band parameters to mineralogy determined for ordinary chondrite meteorites by Sanchez et al. (2020) were used for S-, Sq-, and Q-type asteroids, and Burbine et al.'s (2007) equations for HED meteorites were applied to the V-type asteroids.

3.4.2. OH/H_2O Band

The depth of the OH/H_2O band is calculated after the thermal tail is removed. The robust mean of the data points surrounding 2.9 μm (2.875 μm–2.925 μm) is calculated for both the reflected continuum (RC) and the thermally corrected reflectance spectrum (RB). The band depth (BD) at 2.9 μm is calculated by the formula $\mathrm{BD} = \frac{\mathrm{RC}-\mathrm{RB}}{\mathrm{RC}} * 100$. Band depth is calculated at 2.9 μm because that value is the closest reliable point in the spectrum to the band center ($\sim$2.7 μm) outside of the region with total signal loss due to water vapor in the atmosphere. The error in the band depth was calculated using standard error propagation techniques, and the error from the choice of continuum is added in quadrature as described in

Section 3.3. A band is defined as present if the depth is greater than the 2σ error, and a band is defined as potentially present if the depth is greater than the 1σ error. The shape of the 3 μm band, if present, was characterized by plotting band depths, calculated as described above, at 2.95, 3.0, and 3.05 μm, along with the band depth at 2.9 μm. Connecting the points created a simplified band shape, which was then used to group NEAs with similar band shapes together.

3.5. Statistics

We used the SAS JMP statistics software to conduct statistical analyses in order to search for correlations with band presence and shape type. Specifically, a Student's *t*-test was used to determine whether the mean of the tested continuous variable (diameter, perihelion, etc.) was statistically significantly different between the individual band shape types and between the NEAs with no 3 μm feature. Additionally, the sample used (i.e., all targets, only S-complex, etc.) in the tests was varied to ensure the results were not skewed by S/N or spectral type.

4. Results

We made 44 LXD observations of 29 NEAs (Table 2; all values except taxonomy from JPL Horizons unless otherwise noted) using the methods described above. We obtained prism spectra for all targets except (4) Vesta, (357439) 2004 BL86, (25916) 2001 CP44, (3200) Phaethon, and (85275) 1994 LY. For mineralogical analysis, we used data and/or prism spectra from Frere (2021) for Vesta, Reddy et al. (2015b) for 2004 BL86, and the SMASS-MITHNEOS database for 2001 CP44. Mineralogical analysis was not conducted on Phaethon (B-type) and 1994 LY (X-complex). Additionally, we obtained a prism spectrum for (164121) 2003 YT1 but were unable to collect LXD and therefore 3 μm data owing to poor weather conditions. The observing and band parameters for 2003 YT1 are listed in Tables 1 and 3, respectively, but this object is otherwise not discussed in this text. For the NEAs with multiple observations, either only the highest-S/N observation is reported herein, or the observations were made in close enough temporal proximity to allow the data sets to be combined, yielding a higher-S/N spectrum. In the latter case, all results reported refer to the combined spectrum, though all observations used to create the final spectrum are listed in Table 1. Taxonomic classifications were made from the measured prism spectra using the MIT SMASS Bus-DeMeo classification online tool, and we checked and refined our classification using visual comparison to the standard taxonomic types and results from running other available spectra of our targets in the SMASS-MITHNEOS database through the MIT SMASS Bus-DeMeo online tool (DeMeo et al. 2009) to reduce potential inaccuracy in the classification tool caused by noise and/or truncated spectra. The classifications for several NEAs still retain some ambiguity among specific spectral subtypes. Three NEAs exhibit an absorption feature near 3 μm detected at greater than 2σ. Five NEAs exhibit "possible" features for which the detections are between 1σ and 2σ. Twenty-one NEAs do not exhibit a detectable 3 μm feature. Ten of these have S/N that is so low that the limit on detection is not terribly meaningful (i.e., 1σ limit on band depth is greater than 5%; Table 3), but 11 spectra have high enough S/N that the nondetections are meaningful in the context of the absence of volatiles from those surfaces.

4.1. Positive Detections

The three NEAs with a 3 μm feature are (433) Eros, (1036) Ganymed, and 2014 JO25 (Figure 3). Two of the objects have been observed multiple times and by multiple observers in this wavelength range (Ganymed and Eros; Wigton 2015; Rivkin et al. 2018). 2014 JO25 is the smallest of these three NEAs ($D \sim 0.8$ km[5]) and has not been previously studied in this spectral region. It has a band depth of 6.0% ± 2.9%. Eros is the second-largest NEA, with a mean diameter of 16.84 ± 0.06 km (Yeomans et al. 2000). It was observed seven times by Rivkin et al. (2018) and eight times in this study; the observation made on 2019 January 4 is the only one reported here (a follow-up paper will present the other spectra and analyze variations). Ganymed, the largest NEA ($D = 37.675 \pm 0.399$ km; Mainzer et al. 2016), was observed nine times by Rivkin et al. (2018) and four times in this study; only the observation made on 2011 October 19 is reported here (a follow-on paper will present the other spectra and analyze variations). The Eros and Ganymed spectra reported are generally representative of other spectra collected of these two NEAs. Rivkin et al. (2018) found both Eros's and Ganymed's band depth to vary, ranging from 0.0% ± 2.0% to 5.0% ± 2.7% for Eros and from 0.0% ± 1.5% to 6.2% ± 2.1% for Ganymed. Our band depths for both objects fall within those ranges: Eros's band depth is 2.5% ± 1.1%, and Ganymed's is 2.7% ± 1.3%. The three objects' spectra exhibit three different band shape types, which will be discussed in Section 5.1.2.

Both MBAs observed, (4) Vesta and (349) Dembowska, also have a definitive 3 μm feature. Vesta, the archetypal V-type asteroid, has been studied in the 3 μm spectral region by ground- and space-based instruments numerous times (e.g., Hasegawa et al. 2003; Vernazza et al. 2005; De Sanctis et al. 2012; Reddy et al. 2012a). Our observation yielded a band depth of 2.4% ± 0.9%, which is comparable to the depths seen by Hasegawa et al. (2003) and De Sanctis et al. (2012). Dembowska, a large R-type asteroid, has not been studied in the 2 μm–4 μm spectral region. Our observation yielded a band depth of 5.4% ± 2.1%.

4.2. Potential Detections

The five NEAs that potentially have a 3 μm feature are (214088) 2004 JN13, (159402) 1999 AP10, (3122) Florence, (96590) 1998 XB, and (163373) 2002 PZ39 (Figure 4). All five have depths that are greater than the 1σ error bars but less than the 2σ error bars and have spectral shapes that suggest an absorption feature. Nevertheless, given the low S/N of these spectra, we are not completely confident that the features are real. 2004 JN13's band has a different shape from any other target and has a band depth of 3.1% ± 3.1%.

The other four NEAs with a potential detection exhibit the same band shape type as each other. 1999 AP10 has the strongest band of the four, with a band depth of 3.5% ± 1.8%, and is an Sq-type asteroid. Florence is also an Sq-type and has a band depth of 1.9% ± 1.9%. The remaining two NEAs with a potential band are Q-type asteroids: 1998 XB has a band depth of 6.4% ± 4.6%, and 2002 PZ39 has a band depth of

[5] https://cneos.jpl.nasa.gov/news/news196.html

Table 2
NEA and MBA Physical and Orbital Characteristics

Object		D (km)	Tax.	q (au)	Q (au)	Orb. Per. (yr)	Rot. Per. (hr)	Albedo
433	Eros	16.8	S	1.13	1.78	1.76	5.27	0.25
1036	Ganymed	37.7	S/Sr	1.24	4.09	4.35	10.30	0.24
1627	Ivar	9.1	S/Sq	1.12	2.60	2.54	4.80	0.15
1685	Toro	3.4	Sq	0.77	1.96	1.60	10.20	0.31
1981	Midas	3.4	V	0.62	2.93	2.37	5.22	⋯
3122	Florence	4.9	Sq	1.02	2.52	2.35	2.36	0.23
3200	Phaethon	6.3	B	0.14	2.40	1.43	3.60	0.11
5143	Heracles	4.8	Q	0.42	3.25	2.48	2.71	0.23
6063	Jason	1.4	Sq	0.52	3.91	3.29	48.6	0.21
25916	2001 CP44	5.7	Sq	1.28	3.84	4.10	4.60	0.18
54789	2001 MZ7	1.6	Xe	1.27	2.29	2.37	37.57	0.86
66146	1998 TU3	2.9	Sq/Q	0.41	1.17	0.70	2.38	0.22
66391	Moshup	1.3	Q	0.20	1.08	0.51	2.76	0.23[a]
68950	2002 QF15	1.7	Sr	0.69	1.42	1.09	47	0.18
85275	1994 LY	2.5	X	1.05	2.73	2.60	2.70	0.09
96590	1998 XB	0.9	Q	0.59	1.23	0.87	520	0.49
143404	2003 BD44	∼1.4[b]	Sq/Q	0.77	3.16	2.76	78.64	⋯
144332	2004 DV24	1.2[c]	Sq	1.01	1.83	1.70	7.99	0.22[c]
153201	2000 WO107	0.5	X	0.20	1.62	0.87	4.8[d]	0.13[d]
159402	1999 AP10	1.0[c]	Sq	1.01	3.74	3.66	7.91	0.40[c]
163373	2002 PZ39	0.5[c]	Q	0.67	2.27	1.78	∼149[e]	0.17[c]
163696	2003 EB50	1.6[c]	V	0.76	2.39	1.97	62.4	0.12[c]
194126	2001 SG276	0.6[c]	Sq	1.08	1.79	1.71	5.09	0.30[c]
214088	2004 JN13	2.4	Sq	0.87	4.87	4.87	6.34	0.25
285944	2001 RZ11	1.0	V	1.08	3.30	3.24	2.25	0.41
332446	2008 AF4	0.2[c]	S/Sr	0.81	1.95	1.63	⋯	0.40[c]
357439	2004 BL86	0.3[f]	V	0.90	2.11	1.84	2.62	0.40[f]
454177	2013 GJ35	2[g]	V	1.09	3.19	3.13	⋯	⋯
	2014 JO25	∼0.8[h]	Sr	0.24	3.90	2.97	4.53	0.25[h]
4	Vesta	525.4	V	2.15	2.57	3.63	5.34	0.42
349	Dembowska	139.8	R	2.66	3.19	5.00	4.70	0.38

Notes.
[a] Mainzer et al. (2019).
[b] https://echo.jpl.nasa.gov/asteroids/2014JO25/2014JO25_planning.html
[c] http://nearearthobjects.nau.edu/neosurvey/results.html
[d] https://echo.jpl.nasa.gov/asteroids/1988XB/1988xb.2020.goldstone.planning.html
[e] https://echo.jpl.nasa.gov/asteroids/2002PZ39/2002PZ39_planning.html
[f] Reddy et al. (2015b).
[g] Warner et al. (2009).
[h] https://cneos.jpl.nasa.gov/news/news196.html

33.8% ± 18.4%. Band shape will be discussed in more detail in Section 5.1.2.

4.3. Nondetections

Of the 21 NEAs without a 3 μm feature, 11 of them have spectra with relatively high S/N that rule out bands of depth a few percent or greater (Table 3; Figure 5(a)). The other 10 have spectra that are too noisy to meaningfully confirm the presence or lack of an absorption in the 3 μm region (Table 3; Figure 5(b)). A band depth error of approximately 5%, which corresponds to an S/N of 15, was chosen as the cutoff between the two abovementioned nondetection groups. Detected features generally have a band depth of less than 5% at 2.9 μm, including as seen by Dawn on Vesta (De Sanctis et al. 2012) and on the Moon in some spectra (Clark 2009; Sunshine et al. 2009 and Pieters et al. 2009 report some deeper features). Additionally, plotting a histogram of S/N averaged over a 0.05 μm wavelength range centered on 2.9 μm showed a gap between spectra with S/N less than 15 and those with higher S/N. The highest-S/N spectra of the noisier group of spectra is 12 ((5143) Heracles), with the next highest being 21 ((194126) 2001 SG276). The nondetection NEAs exhibit a wide range of sizes, spectral types, and orbital characteristics, though the characteristics sampled were restricted by observational requirements (Figure 6).

5. Analysis

5.1. Band Parameter Analysis

5.1.1. Prism Bands

The temperature-corrected band parameters for all olivine- and/or pyroxene-rich targets (S-complex and V-types) are shown in Table 4, as well as red-edge- and S/N-corrected mineralogical determinations using the equations presented in Sanchez et al. (2020) for S-complex objects and Burbine et al. (2007) for V-type objects (see Section 3.4.1). BIC and BAR are plotted in Figure 7 along with different S-complex asteroid

Table 3
NEA and MBA Band Depths and Band Shape Types

	Object	3 μm Band?	Band Shape Type	Band Depth (with 1σ Error)
433	**Eros**	**Yes**	**One**	**2.5 ± 1.1**
1036	**Ganymed**	**Yes**	**Three**	**2.7 ± 1.3**
1627	**Ivar**	**No**	···	**1.7 ± 2.3**
1685	**Toro**	**No**	···	**1.8 ± 3.6**
1981	Midas	No	···	8.4 ± 9.9
3122	**Florence**	**Maybe**	**Four**	**1.9 ± 1.9**
3200	**Phaethon**	**No**	···	**0.5 ± 1.8**
5143	Heracles	No	···	1.9 ± 5.6
6063	Jason	No	···	7.0 ± 11.4
25916	2001 CP44	No	···	8.7 ± 14.0
54789	2001 MZ7	No	···	−1.2 ± 6.2
66146	**1998 TU3**	**No**	···	**−0.9 ± 3.7**
66391	**Moshup**	**No**	···	**0.8 ± 2.4**
68950	2002 QF15	No	···	8.1 ± 6.6
85275	1994 LY	No	···	4.8 ± 18.8
96590	**1998 XB**	**Maybe**	**Four**	**6.4 ± 4.6**
143404	2003 BD44	No	···	8.0 ± 8.9
144332	2004 DV24	No	···	1.6 ± 13.8
153201	**2000 WO107**	**No**	···	**0.4 ± 1.9**
159402	**1999 AP10**	**Maybe**	**Four**	**3.5 ± 1.8**
163373	**2002 PZ39**	**Maybe**	**Four**	**33.8 ± 18.4**
163696	**2003 EB50**	**No**	···	**−2.4 ± 2.4**
194126	**2001 SG276**	**No**	···	**2.2 ± 4.2**
214088	**2004 JN13**	**Maybe**	**Two**	**3.1 ± 3.1**
285944	**2001 RZ11**	**No**	···	**−0.2 ± 2.1**
332446	2008 AF4	No	···	1.8 ± 7.8
357439	**2004 BL86**	**No**	···	**0.1 ± 1.0**
454177	**2013 GJ35**	**No**	···	**0.1 ± 3.0**
	2014 JO25	**Yes**	**Four**	**6.0 ± 2.9**
4	**Vesta**	**Yes**	**Three**	**2.4 ± 0.9**
349	**Dembowska**	**Yes**	**Three**	**5.4 ± 2.1**

Note. Objects in bold have absorption bands detected at the $\geqslant 1\sigma$ level and/or a band depth uncertainty of <5%.

subtypes defined by Gaffey et al. (1993). Two S-complex NEAs do not plot in the S(IV) region (Ganymed and 2002 QF15), which is the only region for which the Sanchez et al. (2020) mineralogy equations are intended. Though extrapolating the linear equation for ol/(ol+pyx) should result in greater accuracy for that quantity than extrapolating the parabolic equations for Fa and Fs, using these equations for Ganymed and 2002 QF15 yields Fa and Fs values consistent with H ordinary chondrites (see Figures 3(a) and 4(a) in Dunn et al. 2010 and Figure 3 in Sanchez et al. 2019), while the ol/(ol+pyx) results are not (see Figure 1(a) in Dunn et al. 2010). Equations derived specifically for S-complex asteroids that do not plot in the S(IV) region would likely produce more accurate mineralogical determinations for these two NEA spectra.

Six NEAs plot in the BA (basaltic achondrite) region (V-types; (68950) 2002 QF15 is an Sr-type but also plots in this region), one in the S(VI) region (Sr- and Sv-types), and 16 in the S(IV) region (pyroxene-poor members of the S-complex). Two of those 16 NEAs lie along the boundary with the lower S(III) region and one close to the boundary with the S(VI) region. Two plot above the S(IV) region, one of which lies close to the edge of the S(II) region. Seven of the eight NEAs with a detected or potentially detected 3 μm band plot in the S(IV) region, though 2014 JO25 is the NEA on the border between the S(IV) and S(VI) regions. (1036) Ganymed is the one NEA with a (potential) feature not in the S(IV) region and is instead in the S(VI) region, meaning all eight NEAs with a (potential) feature are S-complex asteroids. Of those in the S(IV) region, three NEAs plot in the LL ordinary chondrite section, 10 plot in the L ordinary chondrite section, and three plot in the H ordinary chondrite section, as defined by Dunn et al. (2010).

Our band parameters generally match or are close to previously published results, with some exceptions (Thomas et al. 2014; Dunn et al. 2013; Popescu et al. 2014; Reddy et al. 2022; Aznar et al. 2019; Ieva et al. 2015; Leith et al. 2017). Ganymed's BAR varies in previously published data, causing it to often plot in the S(IV) region, in addition to the S(VI) region (Thomas et al. 2014). Thomas et al. (2014) attribute some of this variation to phase angle, but it is unclear whether any of the remaining variation is due to spatial variability. We will investigate potential spatial variability on Ganymed, as well as on Eros and Florence, in an upcoming paper. Our calculated BAR values for Heracles, 2002 QF15, and 2014 JO25 are generally higher than previously published values (e.g., Thomas et al. 2014; Popescu et al. 2014; Dunn et al. 2013; Aznar et al. 2019), significantly so for the latter two objects.

5.1.2. OH/H_2O Band

The eight NEAs that have or likely have a 3 μm absorption feature exhibit four different band shape types (Figure 8). Takir & Emery (2012) classified OH/H_2O 3 μm bands on 28 large, low-albedo (C-complex and P-type) MBAs based on band shape and center (see Figures 7 and 9–11 in Takir & Emery 2012), and their classification also consisted of four groups, though the two sets of groups do not align completely. Eros exhibits a fairly linear feature that sharply increases from ~2.85 μm to the reflected continuum around 3.2 μm. This band shape type (Figure 8(a)), named here "Type 1," is nearly identical in shape to the Takir & Emery (2012) "sharp" group, which composed over 50% of their sample, though their reported feature was typically wider, extending to approximately 3.5 μm, and significantly deeper. This feature is attributed to hydroxide, in the form of either hydrated minerals like phyllosilicates or molecular OH (e.g., Lebofsky 1980). 2004 JN13 also exhibits a feature similar to our Type 1 and the Takir & Emery (2012) sharp group, though it is much narrower and slightly steeper. This "Type 2" feature is typified by a linear feature that sharply increases from ~2.85 μm to the reflected continuum around 3.05 μm (Figure 8(b)).

Ganymed exhibits a rounded, bowl-like feature that is shallow and slightly curved from ~2.85 to ~3.1 μm before curving more sharply to meet the continuum at ~3.2 μm (Figure 8(c)). Labeled as Band Shape Type 3, Ganymed's feature is most similar to the Takir & Emery (2012) rounded group, whose feature is attributed to water ice, though our Type 3 does not match Takir & Emery's classification system as well as our Type 1. Vesta and Dembowska, the two MBAs observed by this study, also exhibit Band Shape Type 3. The other five NEAs—2014 JO25, 1999 AP10, Florence, 1998 XB, and 2002 PZ39—exhibit Band Shape Type 4, which is unlike any group described by Takir & Emery (2012), though it, like our Type 3, is most similar to the Takir & Emery (2012) rounded group. Type 4 is similar to Type 3 but is narrower, with a deeper and more severely curved bowl shape from ~2.85 μm to the reflected continuum at ~3.05 μm (Figure 8(d)). Similar to the Takir & Emery (2012) rounded

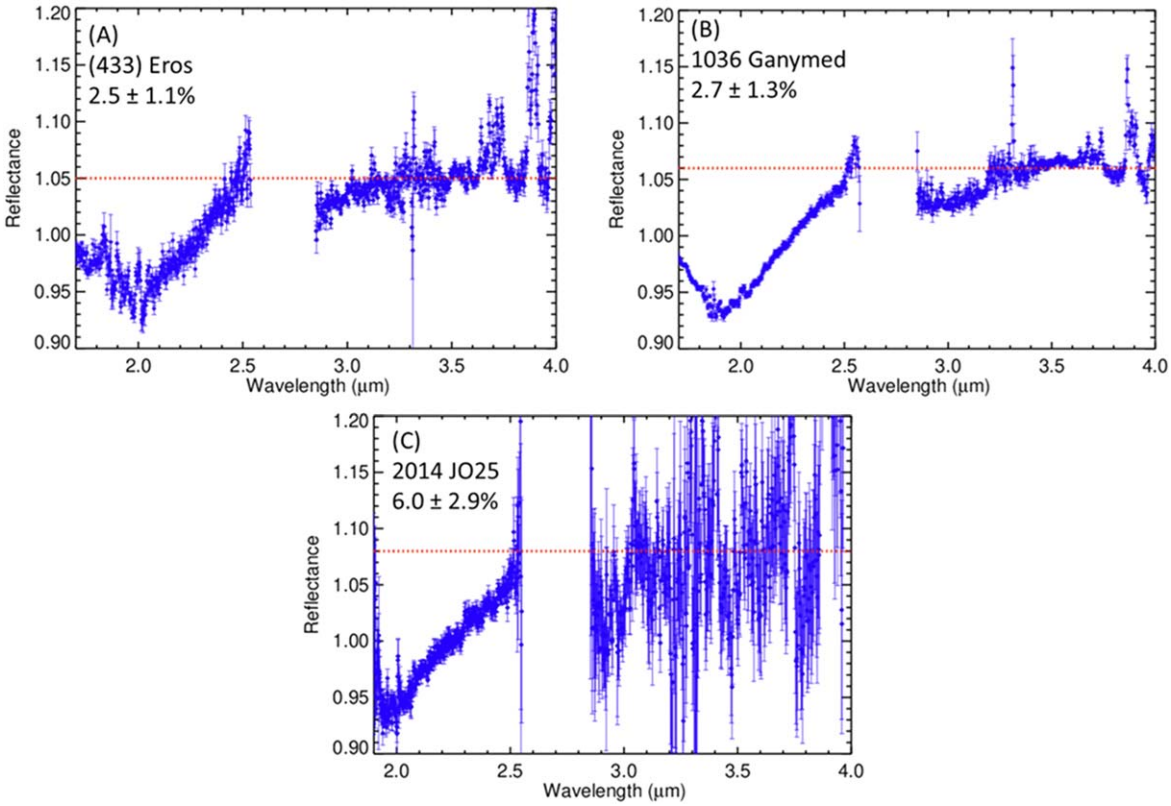

Figure 3. Three NEAs with definite features. The blue points with error bars represent the thermally corrected reflectance spectrum, and the red dashed line represents the reflected continuum. (a) (433) Eros as observed on 2019 January 4. (b) (1036) Ganymed as observed on 2011 October 19. Data points shown for Eros and Ganymed from 1.7 to 2.55 μm are from prism due to noise in the LXD data. (c) 2014 JO25 as observed on 2017 April 22; spectrum longward of 2.85 μm binned by a factor of 2.

group, Band Shape Types 3 and 4 increase slightly in reflectance around 2.8 μm, though this pattern is only evident in binned spectra. The Takir & Emery (2012) Ceres-like feature (broad absorption band from ~2.8 to 3.7 μm with a superimposed band at 3.05 μm) and Europa-like feature (similar to Ceres-like but with a superimposed band centered at 3.15 μm) are not represented in our sample of NEAs. The four band shape types are summarized in Table 5.

5.2. Target Comparisons

We searched for trends between the presence of a 3 μm band and several physical and orbital characteristics in order to identify any differences between the population of NEAs that have and do not have a 3 μm feature. Quantities such as perihelion, composition (including spectral type, band slopes, and mineralogy from band parameters), diameter, aphelion, rotation rate, heliocentric distance, Earth and Jupiter minimum orbit intersection distance, orbital eccentricity, orbital inclination, orbital period, and time since perihelion passage were compared against the band depth at 2.9 μm. Of those, only aphelion (Figure 12) and composition show strong trends. Diameter (Figure 9), perihelion, orbital period, and albedo appear to be weakly correlated with the presence of a 3 μm band.

The two largest NEAs (Eros and Ganymed, mean diameters of ~17 and ~38 km), both in our sample and in the entire population of NEAs, exhibit a 3 μm feature, while most of the other NEAs in our sample with no feature are smaller than 5 km. However, the other six NEAs with (potential) features are also smaller than 5 km. The possible trend with diameter is therefore nonunique, even though the diameters of Eros and Ganymed are large enough to statistically differentiate them from the mean diameters of the other NEAs. With respect to perihelion distance, most of the NEAs with no 3 μm feature have $q \lesssim 1$ au, while both Eros's and Ganymed's perihelia are greater than 1.1 au. This apparent trend, like with diameter, is also nonunique, as the other six NEAs with a (potential) feature also have $q \lesssim 1$ au. Likewise, the objects with the largest orbital periods (~4.6 yr), 2004 JN13 and Ganymed, both exhibit a (potential) feature, while the rest of the NEAs in our sample have orbital periods statistically significantly shorter, regardless of the presence of a band. No other trends discussed in this section were statistically significant.

The nonunique trends in diameter (Figure 9), perihelion, and orbital period discussed above, as well as in albedo, are slightly strengthened when considering only the NEAs exhibiting Band Shape Type 4 and those with no band, particularly when the population of NEAs with no band is limited to certain subsets (Figure 10). These trends are strongest when comparing the Band Shape Type 4 NEAs to the S-complex NEAs with higher-S/N spectra. Higher-S/N NEAs with no band tend to be larger than the Type 4 NEAs, over two times larger in the case of higher-S/N S-complex NEAs with no band, but the 1σ error bars on these means suggest that diameter is only weakly correlated with the presence of a band. More observations are required to determine whether this diameter trend is real or a result of larger objects being brighter, resulting in higher-S/N spectra. Similarly, the Type 4 NEAs tend to have slightly larger perihelia, but the substantial overlap in values between the Type 4 NEAs and those higher-S/N NEAs with no band weakens the significance of perihelion. Type 4 NEAs also tend to have larger orbital periods and albedos than higher-S/N

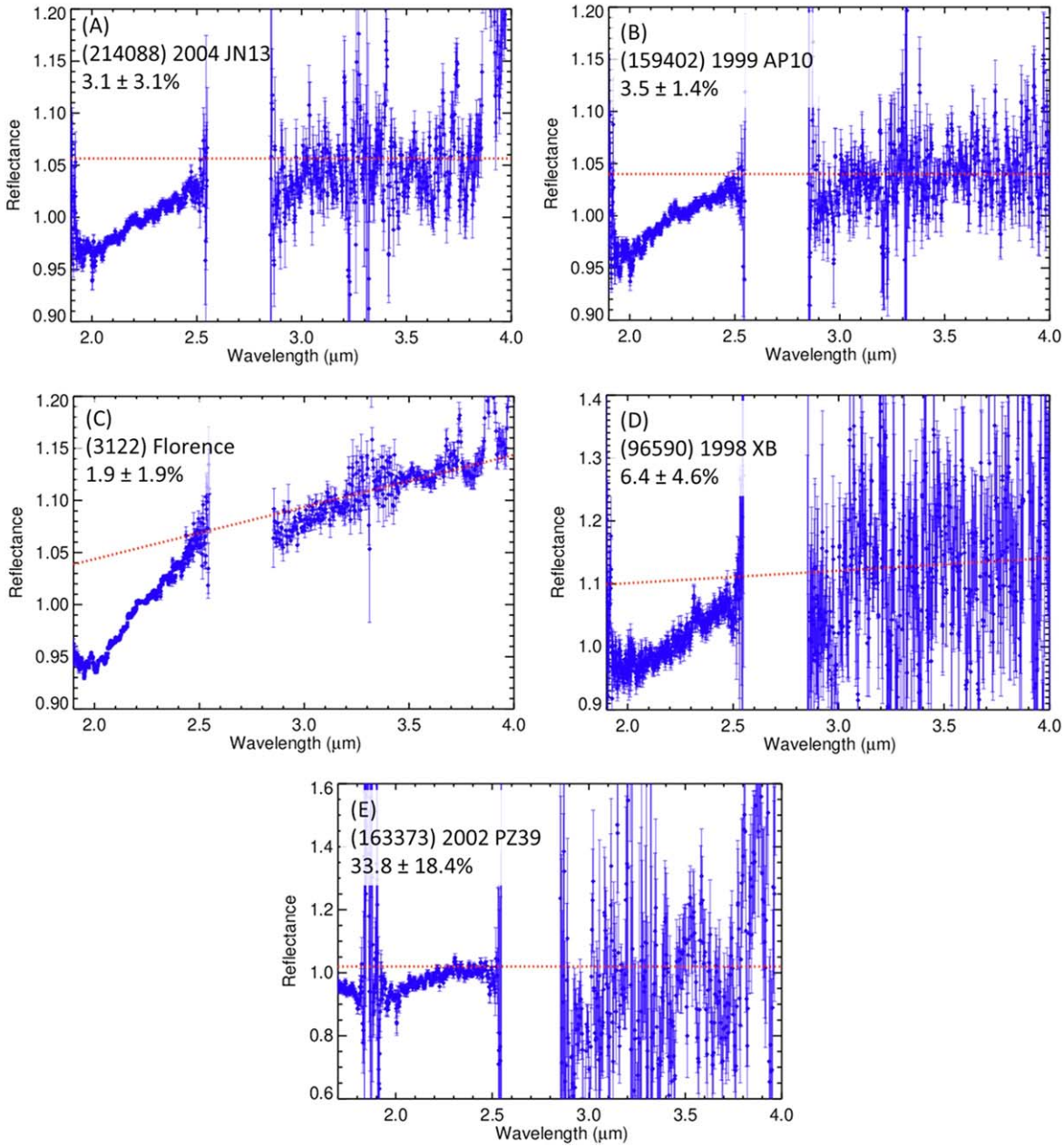

Figure 4. Five NEAs with potential features. (a) (214088) 2004 JN13 as observed on 2014 November 30; spectrum longward of 2.85 μm binned by a factor of 2. (b) (159402) 1999 AP10 as observed on 2020 October 8/9; spectrum longward of 2.85 μm binned by a factor of 2. (c) (3122) Florence as observed on 2017 September 4; spectrum longward of 2.85 μm binned by a factor of 3. (d) (96590) 1998 XB as observed on 2016 November 27; spectrum longward of 2.85 μm binned by a factor of 2. (e) (163373) 2002 PZ39 as observed on 2020 February 12; spectrum binned by a factor of 3.

S-complex NEAs with no band, as the means are 74% and 35% larger, respectively.

Trends in band presence with composition and aphelia are much more robust. As described in Section 5.1.1, all eight NEAs with a (potential) feature are in the S-complex (Figure 11): one is an S-type, three are Sq-types, two are Sr-types, and two are Q-types. We observed one C-complex NEA, three X-complex NEAs, and five V-type NEAs, none of which exhibit a feature in the 3 μm region, though one of the V-types and two of the X-complex NEAs have band depth uncertainties larger than the cutoff described in Section 4.3. When restricting the sample set to only those NEAs in the S-complex with higher-S/N spectra, only 4 of the 12 NEAs show no indication of a 3 μm band. No trend in Fa, Fs, or olivine ratio with band presence or shape is detected.

The trend with aphelia is slightly more complicated but still evident when looking only at higher S/N (as defined in Section 4.3) S-complex NEAs (Figure 12). All four asteroids with $Q > 3$ au exhibit a (potential) 3 μm absorption feature. Six of the eight NEAs with a (potential) feature have aphelia greater than 2.06 au, which means they enter the main belt (defined here as the location of the 4:1 resonance with Jupiter), compared to only one NEA out of four without a feature. Using aphelia to calculate the estimated minimum surface temperature on these asteroids shows that the NEAs with Band Shape Type 4 tend to achieve colder surface temperatures than

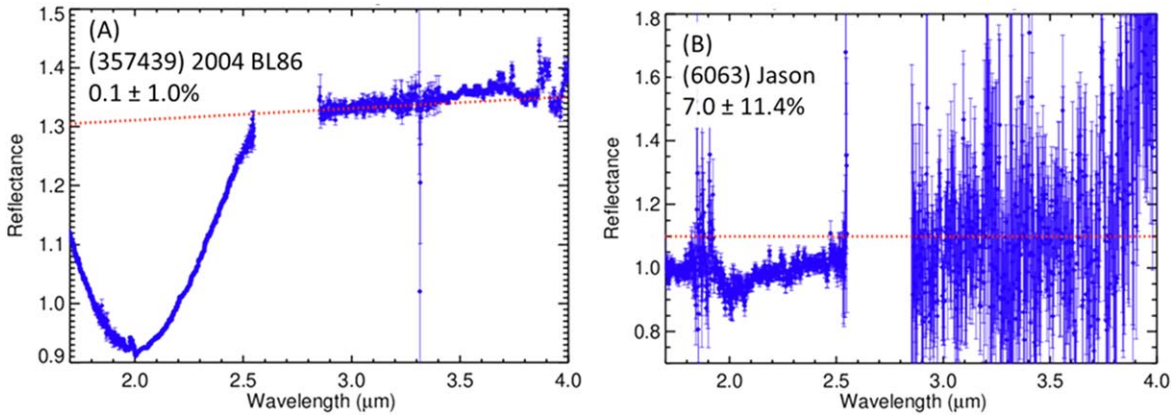

Figure 5. (a) (357439) 2004 BL86 as observed on 2015 January 27 as an example of a high-S/N spectrum showing no detectable absorption feature. (b) (6063) Jason as observed on 2017 June 7 as an example of a low-S/N spectrum that cannot be used to detect a band with a depth of a few percent typical of OH/H_2O.

Table 4
NEA and MBA Band Parameters

S-Complex Asteroids							
Object		Fa	Fs	ol/ol+pyx	BIC	BIIC	BAR
433	Eros	28.2 ± 2.5	23.7 ± 1.8	0.622 ± 0.040	0.972 ± 0.013	2.012 ± 0.006	0.447 ± 0.009
1036	Ganymed[a]	18.8 ± 2.1	17.2 ± 1.5	0.436 ± 0.041	0.920 ± 0.003	1.960 ± 0.001	1.269 ± 0.030
1627	Ivar	25.4 ± 2.3	21.8 ± 1.6	0.621 ± 0.040	0.953 ± 0.007	1.996 ± 0.002	0.451 ± 0.003
1685	Toro	29.3 ± 2.1	24.6 ± 1.5	0.623 ± 0.040	0.985 ± 0.009	2.063 ± 0.002	0.442 ± 0.002
3122	Florence	29.8 ± 2.0	24.9 ± 1.4	0.652 ± 0.040	0.991 ± 0.004	2.016 ± 0.002	0.317 ± 0.004
5143	Heracles	24.7 ± 2.0	22.0 ± 1.4	0.606 ± 0.040	0.954 ± 0.001	1.945 ± 0.003	0.513 ± 0.004
6063	Jason	26.5 ± 2.0	22.6 ± 1.4	0.583 ± 0.040	0.960 ± 0.002	2.017 ± 0.006	0.610 ± 0.016
25916	2001 CP44[b]	30.7 ± 2.0	25.5 ± 1.4	0.650 ± 0.043	1.031 ± 0.008	1.961 ± 0.035	0.334 ± 0.150
66146	1998 TU3	27.3 ± 2.0	23.1 ± 1.4	0.644 ± 0.040	0.965 ± 0.002	1.998 ± 0.002	0.351 ± 0.007
66391	Moshup	23.2 ± 2.0	20.3 ± 1.4	0.574 ± 0.040	0.940 ± 0.001	1.977 ± 0.004	0.689 ± 0.009
68950	2002 QF15[a]	19.8 ± 2.1	17.9 ± 1.4	0.345 ± 0.042	0.925 ± 0.002	1.965 ± 0.007	1.654 ± 0.058
96590	1998 XB	24.9 ± 2.0	21.5 ± 1.4	0.605 ± 0.040	0.950 ± 0.001	2.101 ± 0.001	0.517 ± 0.008
143404	2003 BD44	27.6 ± 2.0	23.4 ± 1.4	0.630 ± 0.040	0.968 ± 0.002	1.981 ± 0.004	0.410 ± 0.012
144332	2004 DV24	29.3 ± 4.3	24.5 ± 3.0	0.655 ± 0.042	0.985 ± 0.036	2.110 ± 0.032	0.307 ± 0.045
159402	1999 AP10	24.6 ± 2.0	21.3 ± 1.4	0.560 ± 0.040	0.948 ± 0.001	1.956 ± 0.014	0.748 ± 0.012
163373	2002 PZ39	27.7 ± 2.0	23.4 ± 1.4	0.617 ± 0.041	0.969 ± 0.003	2.019 ± 0.013	0.467 ± 0.028
194126	2001 SG276	30.7 ± 2.0	25.4 ± 1.4	0.654 ± 0.040	1.016 ± 0.003	2.021 ± 0.002	0.308 ± 0.005
214088	2004 JN13	28.9 ± 2.0	24.2 ± 1.4	0.618 ± 0.040	0.979 ± 0.003	2.024 ± 0.001	0.462 ± 0.008
332446	2008 AF4	21.1 ± 2.0	18.8 ± 1.4	0.499 ± 0.041	0.930 ± 0.002	1.904 ± 0.014	1.006 ± 0.029
	2014 JO25	20.3 ± 2.9	18.2 ± 2.0	0.474 ± 0.040	0.927 ± 0.009	1.964 ± 0.002	1.109 ± 0.014
V- and R-type Asteroids							
Object		Fs	Wo	Mg #	BIC	BIIC	BAR
1981	Midas	50.3 ± 3.2	12.6 ± 1.1	42.4 ± 1.6	0.942 ± 0.001	1.961 ± 0.003	1.759 ± 0.005
163696	2003 EB50	41.4 ± 3.6	9.2 ± 1.3	53.7 ± 2.8	0.933 ± 0.002	1.918 ± 0.001	1.960 ± 0.004
164121	2003 YT1[c]	43.7 ± 3.2	10.1 ± 1.1	50.8 ± 1.6	0.936 ± 0.001	1.993 ± 0.005	1.889 ± 0.028
285944	2001 RZ11	52.1 ± 3.2	13.3 ± 1.1	40.2 ± 1.6	0.944 ± 0.001	1.975 ± 0.001	1.770 ± 0.002
357439	2004 BL86[d]	45.2 ± 3.0	10.7 ± 1.0	49.0 ± 6.5	0.937 ± 0.005	1.99 ± 0.01	1.89 ± 0.04
454177	2013 GJ35	42.6 ± 3.2	9.6 ± 1.1	52.2 ± 1.6	0.934 ± 0.001	1.992 ± 0.002	1.908 ± 0.017
4	Vesta[e]	45.1 ± 3.2	10.6 ± 1.1	49.0 ± 1.6	0.937 ± 0.001	1.967 ± 0.002	1.917 ± 0.004
349	Dembowska	53.1 ± 3.2	13.7 ± 1.1	39.0 ± 1.6	0.945 ± 0.001	1.919 ± 0.001	0.961 ± 0.003

Notes.
[a] Sr-types that do not plot in the S(IV) region.
[b] Prism spectrum from SMASS-MITHNEOS public database.
[c] Only prism data collected.
[d] Data (except Mg #) from Reddy et al. (2015b).
[e] BIC, BIIC, and BAR from Frere (2021).

the S-complex asteroids without a 3 μm feature. The temperature difference between the two populations is even larger when only considering S-complex asteroids with higher-S/N spectra (see Table 6 for temperatures). Finally, the difference between aphelia and perihelia for Band Shape Type 4 NEAs is almost double that of the no-band higher-S/N

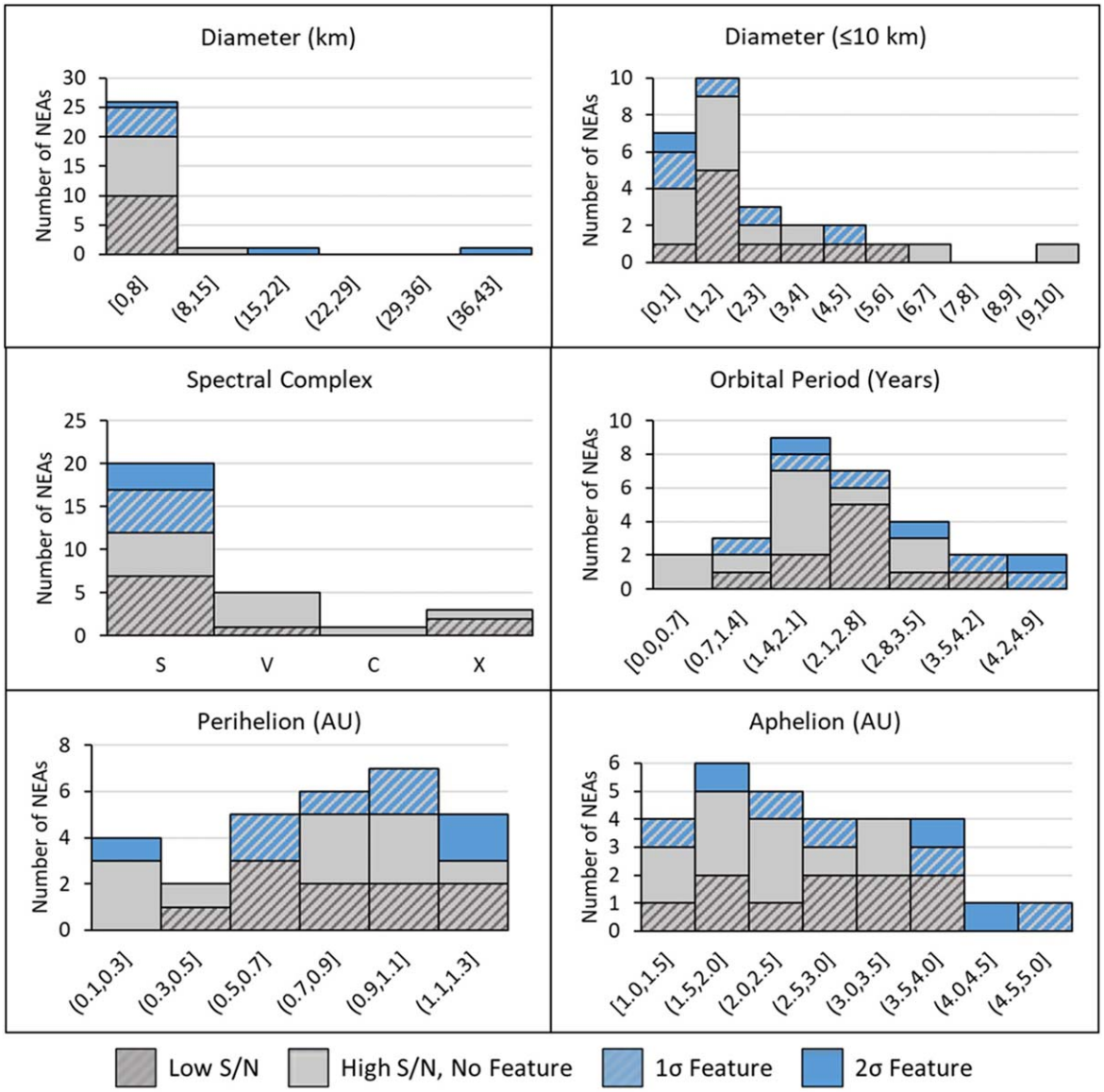

Figure 6. Diameter, spectral complex, orbital period, perihelion, and aphelion distributions of surveyed NEAs. Filled blue represents objects with 2.9 μm bands detected to 2σ, and hashed blue represents the objects with 1–2σ detections. Filled gray represents the NEAs with no detections and upper limits = 5%, and hashed gray represents the objects with low-S/N spectra and no detection.

S-complex NEAs, and that difference is even larger for Ganymed and 2004 JN13. Eros is the only NEA with a (potential) feature whose aphelion–perihelion difference is less than the mean difference for the higher-S/N S-complex asteroids without a feature.

6. Discussion

This survey has shown that OH/H_2O is prevalent but not ubiquitous on NEAs and that NEAs with a 3 μm feature fall into four band shape groups, with some traits shared between all the NEAs with a (potential) 3 μm feature. If the OH/H_2O present on these surfaces was delivered via solar wind hydrogen implantation, OH/H_2O might be expected on all NEA surfaces because they are all impacted by the solar wind. As that is not the case, one or more factors must control the delivery and/or retention of OH/H_2O to/on nominally anhydrous and airless bodies.

6.1. Band Shape

The four band shape types seen in spectra of the eight NEAs with (potential) features suggest different compositions and delivery/retention mechanisms, as seen in MBA surveys (e.g., Takir & Emery 2012; Rivkin 2010).

6.1.1. Type 1—Wide Linear

As previously stated, to date, Band Shape Type 1 (Figure 8(a)) is seen on one NEA, (433) Eros (Figure 3(a)). Eros's feature is present at $>2\sigma$, making it a definitive feature, and it has been detected multiple times. Eros is large ($D \sim 17$ km), has a perihelion of 1.13 au, and is an S-type asteroid. Eros also has the second-smallest aphelion of the eight NEAs with a (potential) feature. The wide, linear, sharp feature possessed by Eros appears most similar to the sharp, Pallas-like band in Takir & Emery (2012) and Rivkin et al. (2019) and also strongly resembles the feature seen on the Moon. Based on the

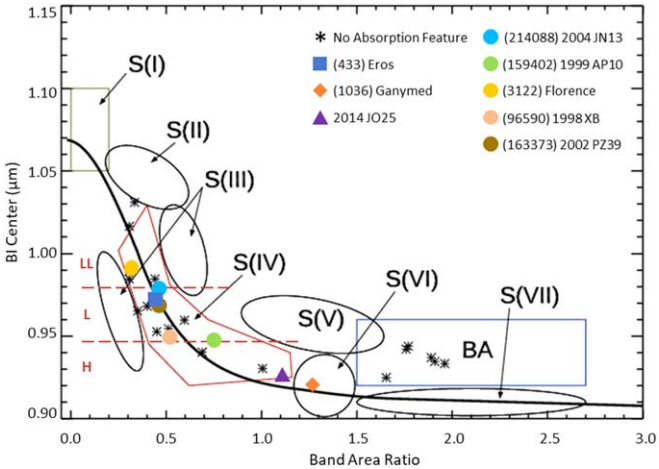

Figure 7. Gaffey et al. (1993) S-subtypes plot with ordinary chondrite lines from Dunn et al. (2010). Our objects with definite and possible bands are shown as colored symbols. Our high-S/N nondetections are shown as black asterisks. Note that both detections and nondetections occur throughout the ordinary chondrite region (SIV), but the basaltic achondrite (BA) region only contains nondetections.

similarity in band shapes, it is likely that Eros and any future NEAs with Band Shape Type 1 have OH, rather than H_2O or some mixture, on their surfaces as determined by Takir & Emery (2012) for the MBAs with sharp features. For the NEAs, we infer that the OH was likely delivered via solar wind hydrogen implantation, the mechanism that delivered OH/H_2O to the Moon. The solar wind origin interpretation of some of the lunar OH is based on the temporal variations seen in the strength of the band as correlated to subsolar position (e.g., Wöhler et al. 2017).

6.1.2. Type 2—Narrow Linear

2004 JN13 (Figure 4(a)) is the only NEA exhibiting Band Shape Type 2 (Figure 8(b)). It is a moderately sized ($D =$ 2.4 km) Sq-type NEA with the largest aphelion of any target studied by this survey. Though somewhat narrower, this feature is similar to that of Band Shape Type 1, indicating that, if real, OH rather than H_2O is likely present. Its perihelion is smaller than Eros's, which, in addition to its extreme aphelion, might explain why 2004 JN13 has a narrower 3 μm band. However, without seeing the entirety of both this band and that of Eros, other explanations for the differences in bandwidth are unclear.

6.1.3. Type 3—Wide Bowl

Only one NEA in our sample, Ganymed (Figure 3(b)), exhibits a shallow, wide, bowl-like feature, which we label Band Shape Type 3 (Figure 8(c)). While no other NEAs exhibit this band shape type, two MBAs were studied using the same methods that do have very similar features: (4) Vesta and (349) Dembowska (Figure 13). Vesta, as mentioned previously, is known to have 3 μm features heavily correlated to exogenous carbonaceous material impacts on its surface (e.g., De Sanctis et al. 2012; Reddy et al. 2012a; McCord et al. 2012). Our ground-based, disk-integrated spectrum of Vesta, like others, confirms the presence of hydrated material (Figure 13; e.g., Hasegawa et al. 2003). Additionally, the ground-based spectrum's 3 μm band shape is nearly identical to the shapes shown by spectra c and d in Figure 2(d) in De Sanctis et al. (2012). Dembowska, an R-type asteroid, shows a similar ground-based, disk-integrated spectrum. Given that R-types are spectrally similar to V-types (e.g., DeMeo et al. 2015) and that Ganymed is an Sr-type with an aphelion larger than either Vesta's or Dembowska's, it is likely that the 3 μm feature on all three is caused by the same mechanism: exogenous carbonaceous material impacts. Given the rough similarity between Ganymed's feature and the rounded feature described by Takir & Emery (2012), H_2O in addition to OH is likely present. However, additional H-bearing species may also be responsible for the features seen on Ganymed, as well as Vesta and Dembowska. Analysis of Dawn spectra of Ceres shows that its feature is best matched by ammonia-bearing clays (e.g., De Sanctis et al. 2018), and analysis of Rosetta spectra of dark refractory material in the nucleus of 67P shows that it is best matched by ammonia-bearing salts (Poch et al. 2020). Potential carbonaceous contamination on Ganymed and other objects could therefore be N-H clays and/or salts from either a Ceres-like or 67P-like object. Further study is needed to determine whether all R/V-type asteroids that have large aphelia and diameters are expected to contain exogenous carbonaceous material and a feature like Band Shape Type 3 or if there is something unique about these three asteroids.

6.1.4. Type 4—Narrow Bowl

Band shape Type 4 (Figure 8(d)) is categorized as a narrow bowl, with a shallowly sloped feature from 2.85 to ~3.0 μm that rapidly increases in reflectance from the band minimum to the reflected continuum between ~3.0 and ~3.05 μm. The five NEAs in this group are 2014 JO25, 1999 AP10, Florence, 1998 XB, and 2002 PZ39 (Figures 3(c) and 4), which are all 5 km or smaller and have perihelia less than 1.02 au. The NEAs that exhibit Band Shape Type 4 also have aphelia greater than 2.06 au, which means they enter the main belt, except 1998 XB, which has the smallest aphelion of the eight NEAs with a (potential) feature of 1.23 au. 2002 PZ39 and 1998 XB are Q-types, Florence and 1999 AP10 are Sq-types, and 2014 JO25 is an Sr-type.

The bowl-like shape of the band likely indicates the presence of H_2O ice, possibly in addition to OH, as suggested in Takir & Emery (2012). Given the shallow nature of the band, OH/H_2O was likely delivered to these objects via solar wind hydrogen implantation, just like for the NEAs with Band Shape Type 1, and/or through exogeneous carbonaceous material, like for Ganymed and Vesta. If the OH/H_2O was delivered via interactions with the solar wind, a different process must also be acting on the surfaces of these NEAs to cause the different band shape. If a process like recombinative desorption is occurring on the NEAs with this band shape, it could explain the bowl-like feature, which, as mentioned above, may be indicative of H_2O, rather than the linear one caused by only solar wind proton bombardment. However, given that all but one of the NEAs in this group enter the main asteroid belt, the possibility for exogenous material is greater than for Eros, which does not interact with the main belt, so it is likely that asteroids with Band Shape Type 4 receive OH/H_2O through multiple mechanisms and from multiple sources.

6.2. Potential Driving Factors

The NEAs with (potential) 3 μm absorption features share several similarities, both within each band type group and all together, notably aphelion and spectral type, with weak trends

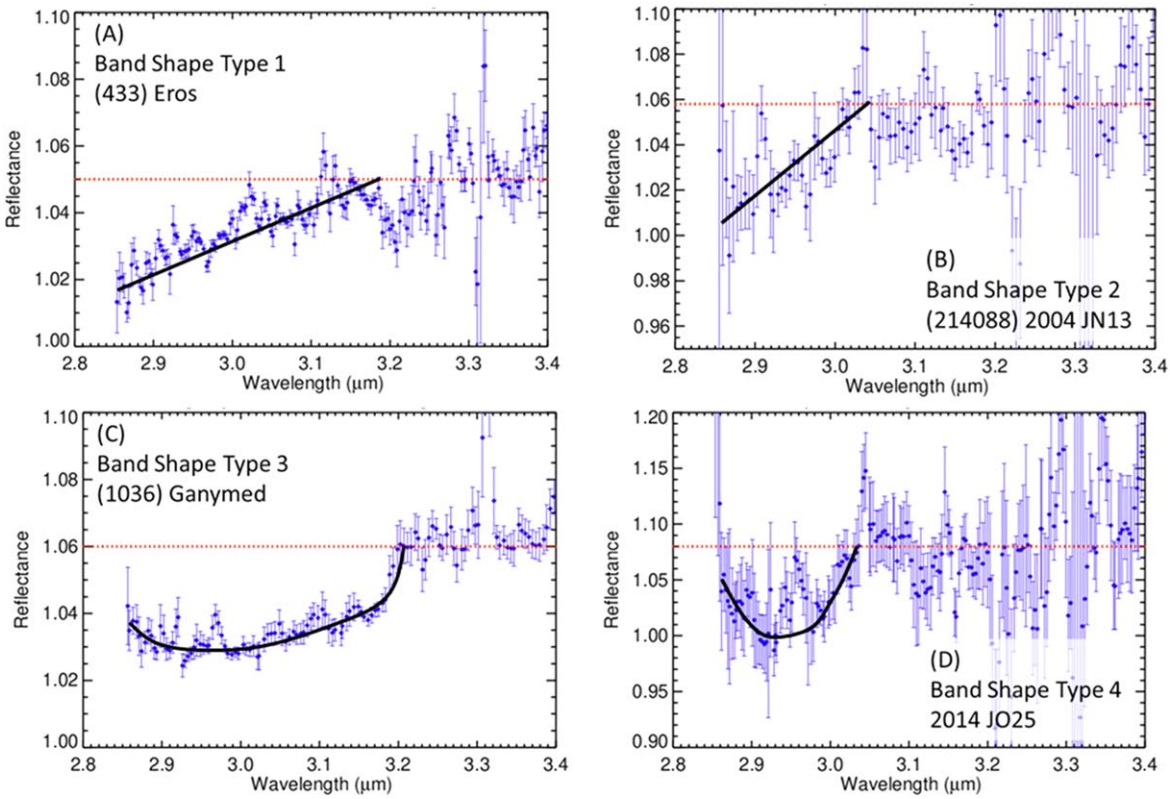

Figure 8. Examples of band shape types seen in this survey. Black curves represent model band shape types. (a) Band Shape Type 1; (433) Eros as observed on 2019 January 4, binned by a factor of 3. (b) Band Shape Type 2; (214088) 2004 JN13 as observed on 2014 November 30, binned by a factor of 5. (c) Band Shape Type 3; (1036) Ganymed as observed on 2011 October 19, binned by a factor of 3. (d) Band Shape Type 4; 2014 JO25 as observed on 2017 April 22, binned by a factor of 3.

Table 5
Descriptions of the Four Band Shape Types

Band Shape Type	Description	NEAs with Band Shape Type	
1	Wide linear: reflectance linearly increases from 2.8 μm to reflected continuum around 3.2 μm	433	Eros
2	Narrow linear: reflectance linearly increases from 2.85 to 2.95 μm, more shallowly linearly increases to reflected continuum around 3.05 μm	214088	2004 JN13
3	Wide bowl: feature shallow and flat from 2.8 to 3.1 μm, reflectance increases nonlinearly to reflected continuum around 3.2 μm	1036	Ganymed
4	Narrow bowl: feature shallow and flat from 2.8 to 3.0 μm, reflectance increases nonlinearly to reflected continuum around 3.05 μm	3122 96590 159402 163373	Florence 1998 XB 1999 AP10 2002 PZ39 2014 JO25

evident in size, perihelion, orbital period, and albedo. Of the numerous other physical and orbital characteristics investigated, only the former two characteristics seem to control OH/H_2O delivery and/or retention, with the latter four appearing to have some degree of influence. However, other NEAs also exhibit one or two of the same characteristics but do not have a 3 μm feature, implying that none of these factors alone determine the presence of a 3 μm absorption feature. Discussing these characteristics in terms of the band type groups clarifies their relationship to the delivery/retention process(es).

6.2.1. Composition and Albedo

All eight NEAs with a (potential) band are S-complex; therefore, they all have regolith primarily composed of olivine and pyroxene. Seven of the eight also plot in the S(IV) ordinary chondrite "boot" on a Gaffey S-subtypes plot (Figure 7). Within the S(IV) region, Florence plots in the LL ordinary chondrite subregion, 1999 AP10 and 2014 JO25 plot in the H ordinary chondrite subregion, and the other five plot in the L ordinary chondrite subregion. Ganymed, the only one of the eight outside the S(IV) region, plots in the S(VI) region, which occurs between the ordinary chondrite "boot" and the basaltic achondrites (BA) region in terms of BAR. Other studies show that Ganymed can also plot in the S(IV)/H-chondrite subregion (e.g., Thomas et al. 2014). As primitive achondrites often share the same region as H-chondrites on a Gaffey plot, the band I and II centers of 1999 AP10, 2014 JO25, and Ganymed were plotted and compared to the results found by Lucas et al. (2018); all three NEAs have BIIC values too high to be considered primitive achondrites. As Eros, the NEA with Band Shape Type 1, is an S-type, 2004 JN13 (Band Shape Type 2) is an Sq-type, Ganymed (Band Shape Type 3) is an S/Sr-type, and the NEAs with Band Shape Type 4 are a mix of Q-, Sq-, and Sr-types, exact spectral type within the S-complex does not seem to influence band presence or shape type. The NEAs in the S-complex with no band are also a mix of the types mentioned. Additionally, calculated values for Fa and Fs content, as well as olivine ratio, show no trends with band

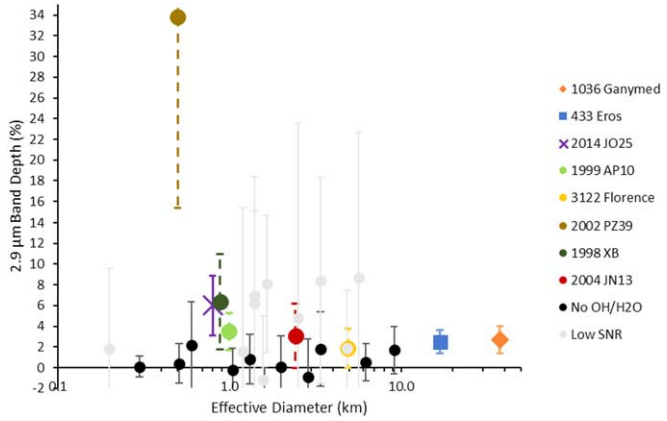

Figure 9. Band depth plotted against effective diameter. Larger NEAs tend to have a 3 μm feature, though the trend is nonunique.

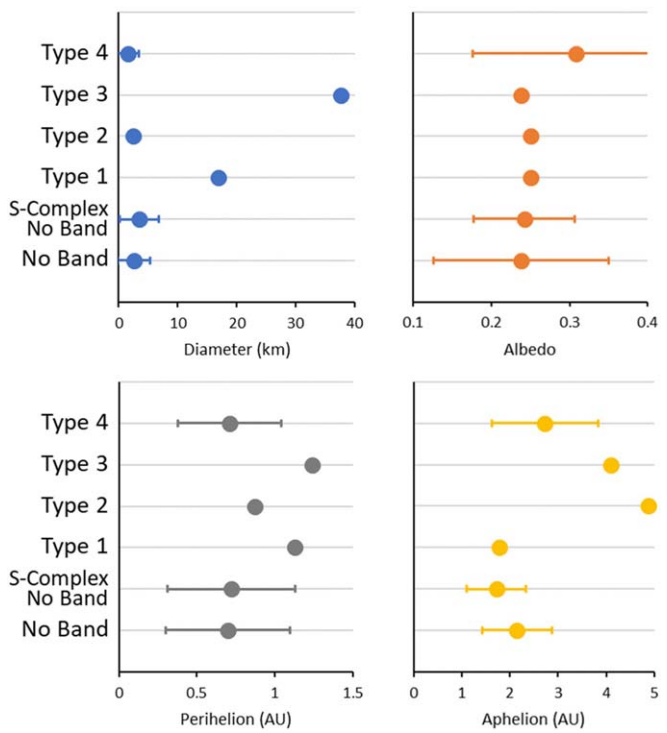

Figure 10. Only higher-S/N NEAs are included in the data points for NEAs with no band. Error bars are standard deviations of the objects of that type. Points with no error bars have only a single object of that type.

depth or band shape type, as stated in Section 5.2. However, the weak association between higher albedo and the presence of a band, particularly a Type 4 feature, suggests a further compositional dependence that will be probed in future studies.

Several NEAs not in the S-complex but possessing similar size and perihelion to the NEAs with a (potential) band do not exhibit a 3 μm absorption feature. The absence of 3 μm features on the V-types studied implies that V-type NEAs do not tend to have OH/H_2O that was delivered via solar wind hydrogen implantation (or any of the other possible sources). This trend may be due to V-types' higher degree of silica saturation, as pyroxene, which dominates V-type surfaces, has a higher silicon-to-oxygen ratio than olivine, resulting in fewer relatively weak, ionic silica tetrahedron-to-metal bonds and more strong, covalent bonds between silica tetrahedra. The mechanical weathering step of the solar wind hydrogen

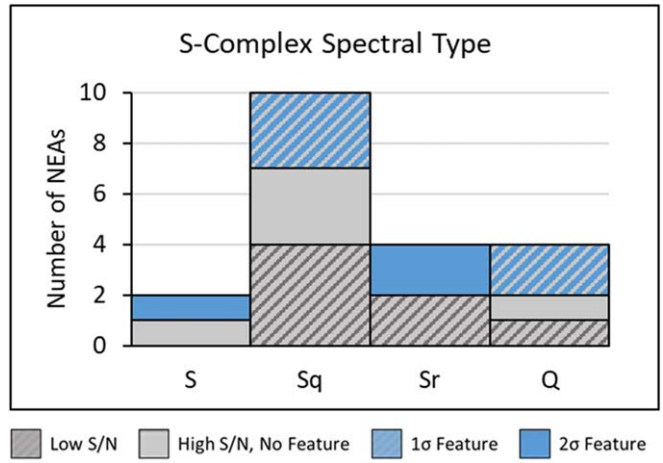

Figure 11. Histogram of S-complex spectral types observed in this study. Filled blue represents objects with 2.9 μm bands detected to 2σ, and hashed blue represents the objects with 1–2σ detections. Filled gray represents the NEAs with no detections and upper limits = 5%, and hashed gray represents the objects with low-S/N spectra and no detection.

implantation process appears to not be as efficient at breaking bonds and implanting hydrogen on V-types as on NEAs in the S-complex. Other studies have shown that irradiation and proton implantation experiments on olivine and pyroxene result in a greater spectral change on the olivine samples than the pyroxene samples (Yamada et al. 1999), suggesting that olivine is more easily changed than pyroxene by such processes. Only one of the three X-complex NEAs observed by this campaign has a higher-S/N spectrum ((153201) 2000 WO107) and, like the V-types, also does not have a 3 μm feature. However, more observations of X-complex NEAs are needed to determine the prevalence of OH/H_2O across the X-complex population.

6.2.2. Aphelion and Orbital Period

Objects that enter the Main Belt are significantly more likely to have a 3 μm band than those that do not, particularly when considering only S-complex NEAs. Six of the eight NEAs with a (potential) feature have aphelia large enough to carry them into the main belt. One of those six (Florence) has an aphelion greater than 2.5 au, and four (Ganymed, 2004 JN13, 1999 AP10, and 2014 JO25) have aphelia greater than 2.8 au, indicating that they travel into the middle and/or outer main belt as defined by the 3:1 and 5:2 Jupiter resonances, respectively.

Approximately 85% of S-complex NEAs in our sample with higher-S/N spectra that enter the main belt have a (potential) 3 μm feature (Figure 12), indicating that S-complex NEAs that enter the main belt are more likely to have OH/H_2O on their surfaces than S-complex NEAs that do not enter the main belt ($Q < 2.06$ au). Additionally, 100% of higher-S/N S-complex NEAs that enter the outer main belt have a 3 μm absorption band. We observed four additional S-complex asteroids that enter the main belt, but the S/Ns of their spectra were too low to determine whether they exhibited a band (these are therefore not shown in Figure 10). Future observations of (5143) Heracles, (6063) Jason, (25916) 2001 CP44, and (143404) 2003 BD44, as well as other NEAs with large enough aphelia, will determine the robustness of this trend. The slight trend in orbital period noted previously is likely only a result of its dependence on aphelion, as no trend was discerned in orbital

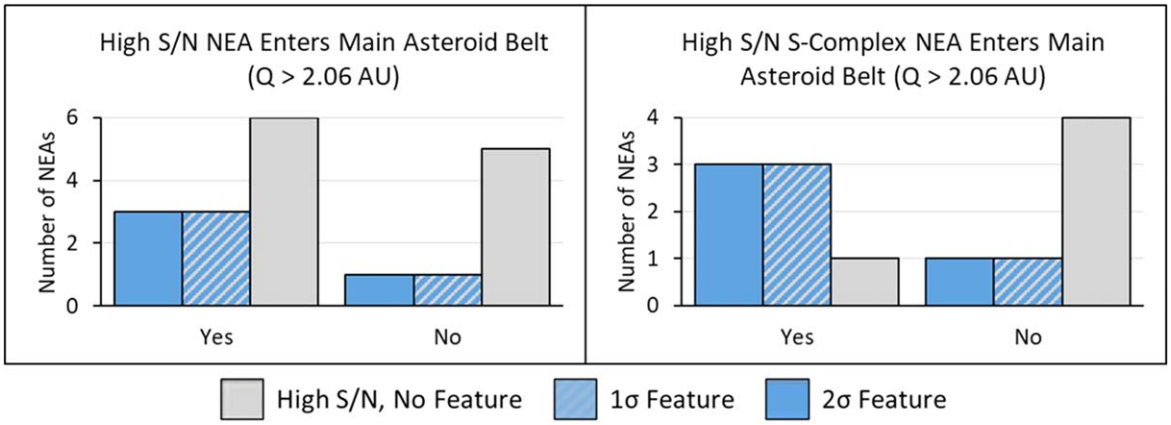

Figure 12. Left: histogram of all higher-S/N NEAs binned by whether they enter the main belt. Right: histogram of higher-S/N S-complex NEAs. Filled blue represents objects with 2.9 μm bands detected to 2σ, and hashed blue represents the objects with 1–2σ detections. Filled gray represents the NEAs with no detections and upper limits = 5%.

Table 6
NEA and MBA Equilibrium and Subsolar Temperatures at Time of Observation, Perihelion, and Aphelion

Object		η	Observation T_{Eq} (K)	Observation T_{SS} (K)	q T_{Eq} (K)	q T_{SS} (K)	Q T_{Eq} (K)	Q T_{SS} (K)
433	Eros	1	259	366	262	370	208	294
1036	Ganymed	1.12	233	330	243	344	134	189
1627	Ivar	1.3	236	333	249	352	163	231
1685	Toro	1.5	248	351	284	402	178	252
1981	Midas	1.3	254	359	329	465	151	214
3122	Florence	1.55	244	346	247	350	158	223
3200	Phaethon	1.6	246	348	671	949	162	229
5143	Heracles	1	257	363	430	608	155	219
6063	Jason	1	280	396	416	588	152	215
25916	2001 CP44	0.8	255	361	262	370	151	214
54789	2001 MZ7	1	226	319	227	321	169	239
66146	1998 TU3	1.4	239	338	400	566	237	335
66391	Moshup	1.6	246	347	552	781	237	335
68950	2002 QF15	1.3	258	364	310	439	216	306
85275	1994 LY	1.6	238	337	245	347	152	215
96590	1998 XB	1.2	244	345	336	475	233	329
143404	2003 BD44	1	261	369	315	445	156	221
144332	2004 DV24	1.3	259	367	260	367	193	273
153201	2000 WO107	1.05	273	386	622	880	218	309
159402	1999 AP10	1.7	232	329	239	338	124	176
163373	2002 PZ39	0.8	290	411	357	505	194	274
163696	2003 EB50	1.65	233	329	276	390	156	220
194126	2001 SG276	1.2	254	359	255	361	199	281
214088	2004 JN13	0.98	262	370	300	424	127	179
285944	2001 RZ11	2.5	167	236	209	295	120	169
332446	2008 AF4	1.6	247	349	274	388	177	250
357439	2004 BL86	1.4	252	357	264	374	173	244
454177	2013 GJ35	1.35	234	332	249	352	146	206
	2014 JO25	0.95	274	387	575	813	143	202
4	Vesta	0.81	183	259	196	277	179	253
349	Dembowska	0.9	158	223	173	244	157	222

period prior to the discovery of the $Q > 2.06$ au boundary in the data, though more observations are required to test this hypothesis.

Entering the main belt might aid in the delivery/retention of OH/H_2O in two ways. First, the likelihood that carbonaceous material will be delivered to an NEA's surface is significantly higher if that NEA spends time in the main belt, particularly the middle and outer main belt, as the middle and outer main belt contains far more carbonaceous material than near-Earth space or the inner main belt do (DeMeo et al. 2015). Second, a large aphelion means that an NEA spends more of its orbit at a lower temperature, where OH/H_2O would be more stable and would then be more easily retained after delivery/creation. While a trend in band depth/shape with orbital phase is not apparent, further work is needed to determine whether the observed features are stable or transient as the NEAs progress along their orbits. As discussed in Section 5.2, the average estimated minimum surface temperature experienced by the NEAs exhibiting Band Shape Type 4 is lower than that of the S-complex NEAs that do not exhibit a feature. It is therefore

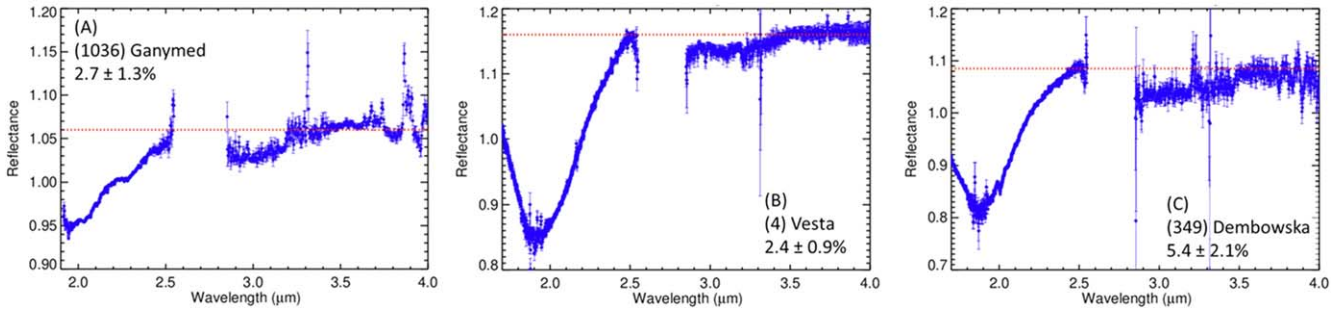

Figure 13. (a) (1036) Ganymed as observed on 2011 October 19. (b) (4) Vesta as observed on 2017 April 2. (c) (349) Dembowska as observed on 2019 May 10. All three asteroids have a similar band shape.

(The data used to create this figure are available.)

likely that the time spent at a cooler temperature, as well as the availability of carbonaceous material, is a driver of OH/H_2O delivery and/or retention. A prediction from this apparent prevalence of 3 μm bands on NEAs that enter the main belt is that main belt S-complex asteroids should show 3 μm bands at a higher rate than NEAs. Nevertheless, two NEAs with (potential) 3 μm features, Eros and 1998 XB, have aphelia less than 2.06 au, implying that 3 μm band presence is not wholly dependent on this supposed interaction with the main belt.

6.2.3. Diameter

Larger objects may be more likely to have a 3 μm absorption feature than smaller objects. As stated in Section 5.2, the diameters of the NEAs with Band Shape Types 1 and 3 (Eros and Ganymed, respectively) are statistically significantly larger than the mean diameter of the NEAs with Band Shape Types 2 and 4 and the NEAs that do not have a 3 μm feature. Of the five asteroids we observed with diameter $\geqslant$5 km, two possess a band, two do not exhibit a 3 μm feature within the level of noise of the data (Ivar and Phaethon), and one has an S/N that is too low to determine the presence of a feature (as defined in Section 4.3). For Phaethon, the absence of a 3 μm band is likely due to its extreme surface temperatures near perihelion (Takir et al. 2020), and future observations of Ivar are required to see whether its lack of feature is intrinsic or variable, as seen by Rivkin et al. (2018) for Eros and Ganymed. For NEAs with $D < 5$ km, only 6 out of 24 exhibit a 3 μm band. Therefore, 50% of NEAs with $D > 5$ km exhibit a 3 μm feature versus 25% of NEAs with $D < 5$ km. However, while size seems to be important in the delivery and/or retention process, it does not control OH/H_2O completely, as the diameters of the NEAs with Band Shape Types 2 and 4 are statistically indistinguishable from those of NEAs with no 3 μm absorption feature.

Size could be important for several reasons. Larger asteroids present a larger projected area, so they are struck by more protons than smaller asteroids, even if the quantity per square meter is the same. Alternatively, and/or additionally, size may be important for OH/H_2O retention because larger asteroids have higher surface gravity, so they may be able to hold on to implanted OH/H_2O more easily than small asteroids. Larger asteroids also tend to be older and have finer-grained regolith, whereas smaller asteroids are rockier (Gundlach & Blum 2013; Delbo et al. 2015). Both Eros's and Ganymed's published thermal inertias are fairly low (e.g., Mueller 2007; Hinkle et al. 2022; Hanuš et al. 2015), suggesting fine-grained regoliths. The efficiency of the mechanical weathering process by which hydrogen is implanted may depend on grain size, as coarser and finer grains physically degrade at different speeds, thereby influencing the efficiency of proton implantation, as discussed in Section 2.2. More research is required to calculate thermal inertias for more NEAs to determine the importance of grain size to OH/H_2O delivery and/or retention.

6.2.4. Perihelion

Lower perihelia may decrease the likelihood of an NEA containing OH/H_2O. The perihelia of NEAs with Types 1, 2, and 3 features are larger than the perihelia of NEAs without a feature (Figure 10), even though the mean perihelia of NEAs with a (potential) 3 μm absorption feature are not statistically significantly different from those without. Nevertheless, the average perihelion of the Type 4 NEAs is indistinguishable from that of the higher-S/N NEAs (Figure 10), meaning any trend in band depth presence with larger perihelion is not strong.

One reason perihelion distance could be related to the delivery and retention of OH/H_2O is the resulting higher maximum equilibrium and subsolar surface temperatures (Table 6). OH/H_2O can dissociate at higher temperatures and therefore leave the surface. Evidence of this process was potentially seen on the Moon, as the lunar 3 μm band depth was found by some to be shallowest at local noon and deepest in the morning and evening (McCord et al. 2011), though new interpretations have since been published (Ruiz et al. 2020; see Section 2.2). As mentioned above, Phaethon's perihelion of 0.14 au leads to a surface temperature of over 1000 K (Takir et al. 2020), which likely means that OH/H_2O is not stable on its surface, or at least not near perihelion.

On the other hand, some NEAs with Band Shape Type 4 have smaller perihelia, so clearly a small perihelion does not preclude the potential for a 3 μm absorption feature. Objects closer to the Sun experience a higher flux of solar wind protons (Nicolaou et al. 2020) and might therefore be expected to experience more hydrogen implantation. However, at small enough perihelia, such as the case for 2014 JO25 and Phaethon, the surface temperature would be high enough to cause some degree of dehydration (Springmann et al. 2019), so even if OH and/or H_2O were being created, it might not be retained. On the other hand, a process such as recombinative desorption could allow for the formation of H_2O even on surfaces with relatively high maximum temperatures, such as experienced by those NEAs with Band Shape Type 4 (Orlando et al. 2018).

Recombinative desorption is a process by which two -OH groups in close proximity thermally react to form H_2O in minerals that have saturated -OH terminal sites and defects (Orlando et al. 2018). Temperatures above 450 K are required for the process to occur; the maximum equilibrium and subsolar temperature on 2014 JO25 are above that threshold, though 1999 AP10 and Florence do not reach such a temperature, regardless of considering the whole-body equilibrium temperature or the peak temperature at the subsolar point (Table 6). However, meteorite impacts can raise the surface temperature of the affected area enough to make recombinative desorption possible (Orlando et al. 2018), and micrometeorite impacts are more likely closer to the Sun than at larger heliocentric distances, even within the main belt (Grün & Zook 1980; Pokorný et al. 2021). Perihelion, as well as maximum surface temperature, therefore seems to be relevant to both OH/H_2O delivery/retention and exact volatile composition and band shape.

6.3. S-complex Nondetections

The bulk of this discussion has focused on the NEAs that have or potentially have a 3 μm feature. However, when only considering the asteroids with band depth errors less than ~5% and removing any NEAs not in the S-complex from this list, we are left with only five S-complex NEAs with higher-S/N spectra that do not have a 3 μm feature: (66391) Moshup, (66146) 1998 TU3, (1685) Toro, (1627) Ivar, and (194126) 2001 SG276. These five objects are indistinguishable from the eight with a (potential) feature in terms of composition, diameter, and perihelion. The question then becomes why these five S-complex NEAs do not have a feature, rather than why the eight S-complex asteroids with higher S/N do.

The most likely explanation for the lack of a feature on these five objects is their relatively low aphelia. Four of the five NEAs do not enter the main belt, and the remaining object, Ivar, does not enter the outer belt. Considering that ~85% of higher-S/N S-complex NEAs that enter the main belt have a 3 μm absorption feature and ~67% of higher-S/N S-complex NEAs that do not enter the main belt do not have a 3 μm absorption feature, entering or not entering the main belt appears to be a primary driver on the presence of OH/H_2O on NEAs. It will be interesting to reobserve Ivar at different orbital and rotational phases to see whether Ivar's band depth varies, as Rivkin et al. (2018) showed for Eros and Ganymed, or whether its lack of feature is inherent. If the latter is true, future observations will help elucidate other drivers of OH/H_2O delivery and/or retention.

6.4. Observational Bias

Though we observed every NEA bright enough to search for a 3 μm feature over the course of five years (when the weather cooperated), observational bias still exists. Perhaps most obviously, given that we had a brightness requirement and we sampled known NEAs, which from the ground are discovered based on visible detections, our sample is biased to higher-albedo objects. Our targets sample a wide range of perihelia, from 0.14 au (3200 Phaethon) to 1.3 au (Figure 6), the limit that defines an NEA. The mode of our perihelia is ~1 au, which matches the overall NEA population (Binzel et al. 2015; Valdes 2019), but our distribution is different. According to CNEOS cumulative discovery statistics,[6] ~8% of NEAs are Atens ($q < 1.0$ au), ~56% are Apollos (1.0 au $< q < 1.017$ au), and ~36% are Amors (1.017 au $< q < 1.3$ au). Our NEAs are ~59% Atens, ~7% Apollos, and ~34% Amors, so our sample is overrepresented in Atens and underrepresented in Apollos. The aphelia distribution of our targets generally matches that of the overall NEA population, as aphelia are fairly uniformly distributed between 1 and ~4.5 au, with a small population of NEAs possessing aphelia up to 6 au (Valdes 2019). As for diameter, only ~4% of all known NEAs are larger than 1 km, and only ~20 of those are larger than or equal to ~5 km in diameter[7]. In contrast, 82% of the NEAs observed in this study are larger than 1 km in diameter, and five of those are larger than or equal to 5 km. We therefore have an observational bias because our study only samples NEAs with diameters well outside the mean. In terms of spectral type, the general NEA population is ~67% S-complex, ~14% C-complex, ~8% X-complex, and ~4% V-types (Binzel et al. 2015). We primarily observed S-complex NEAs (~67%), with five V-types (~18%), three X-complex (~11%), and only one C-complex (~4%; Figure 6). We therefore have little apparent observational bias for S- and X-complex NEAs, though the X-complex is compositionally diverse, but we oversampled V-types and undersampled C-complex NEAs. On a macroscale, our target list is relatively representative of the NEA population as a whole, except in regard to albedo and diameter, and we deviate slightly from the NEA population distribution in terms of perihelion. Given that we are generally not strongly biased in aphelion and composition, and considering that aphelion and composition seem to be more important to the delivery and/or retention of OH/H_2O than albedo, diameter, and perihelion, the observational biases in our sample are not expected to strongly affect our conclusions, though these biases might imply that OH/H_2O is not as prevalent in near-Earth space as our findings suggest. Reducing our observational bias through future observations will improve our understanding of the statistics of 3 μm bands on NEAs and clarify the trends seen by this study.

7. Summary and Conclusions

We conducted a survey of NEAs to determine the prevalence of OH/H_2O in near-Earth space. These nominally anhydrous inner solar system bodies have been subjected to various mechanisms and processes that implant OH/H_2O, such as carbonaceous/cometary material impacts and solar wind hydrogen implantation. We presented here 33 observations of 29 NEAs and two observations of MBAs using NASA's IRTF SpeX NIR spectrometer to further understand the mechanisms and processes involved in OH/H_2O delivery and retention and to determine which factors are most important in controlling the presence of a 3 μm absorption feature.

Of those 29 NEAs, observations of 19 produced high enough S/N spectra to determine the presence or lack thereof of an absorption feature in the 3 μm spectral region. Eight of those exhibit a band to either 1σ or 2σ: (433) Eros, (214088) 2004 JN13, (1036) Ganymed, 2014 JO25, (159402) 1999 AP10, (3122) Florence, (96590) 1998 XB, and (163373) 2002 PZ39. The remaining 11 are featureless at the few percent level. We also identified four band shape types. Eros possesses a wide

[6] https://cneos.jpl.nasa.gov/stats/totals.html
[7] Center for Near Earth Object Studies.

linearly increasing feature similar to the deeper feature seen on (2) Pallas. 2004 JN13 has a similar feature, but it is much narrower. Both NEAs (Band Shape Types 1 and 2) likely contain OH on their surfaces rather than H_2O or some mixture, based on band shape, which was delivered via solar wind hydrogen implantation. Ganymed exhibits a wide, shallow bowl-like feature, likely indicating a mix of OH and H_2O, that is nearly identical in shape to our ground-based observation of (4) Vesta and (349) Dembowska. As Vesta's hydration is known to have an exogeneous carbonaceous material source, Ganymed's OH/H_2O was likely delivered via the same mechanism. The remaining five NEAs exhibit Band Shape Type 4, a narrow bowl-like feature, also likely an indication of a mix of OH and H_2O; however, their shape differs enough from Ganymed's to suggest that the source of their OH/H_2O may be different. A combination of processes likely delivered this volatile, such as solar wind hydrogen implantation in addition to recombinative desorption.

Given that all eight NEAs with a (potential) 3 μm feature belong to the S-complex and that six of them have aphelia large enough to enter the main belt, composition and aphelion appear to be the two most significant driving factors in OH/H_2O delivery and/or retention. V-types' pyroxene-rich composition may not be conducive to OH/H_2O formation/retention. Minor trends with diameter, perihelion, orbital period, and albedo were also identified, though more data are required to determine their importance and untangle competing effects. Not only did our study determine that nominally anhydrous, inner solar system bodies, and therefore near-Earth space in general, contain more OH/H_2O than previously expected, we also found strong trends that can help predict which NEAs that have not yet been observed might contain OH/H_2O on their surfaces. In particular, S-complex NEAs that enter the main belt appear more likely to have a 3 μm feature than not, and future observations will further investigate the reason for this trend.

Visiting Astronomer at the Infrared Telescope Facility, which is operated by the University of Hawaii under contract 80HQTR19D0030 with the National Aeronautics and Space Administration. Taxonomic type results presented in this work were determined, in whole or in part, using a Bus-DeMeo Taxonomy Classification Web tool by Stephen M. Slivan, developed at MIT with the support of National Science Foundation grant 0506716 and NASA grant NAG5-12355. All (or part) of the data utilized in this publication were obtained and made available by the MITHNEOS MIT-Hawaii Near-Earth Object Spectroscopic Survey. The IRTF is operated by the University of Hawaii under contract 80HQTR19D0030 with the National Aeronautics and Space Administration. The MIT component of this work is supported by NASA grant 80NSSC18K0849. This work was supported by NASA grants NNX16AE91G and 80NSSC20K0291.

Appendix

An atlas of all SpeX spectra for the NEAs presented in this work is available in the online figure set associated with Figure A1.

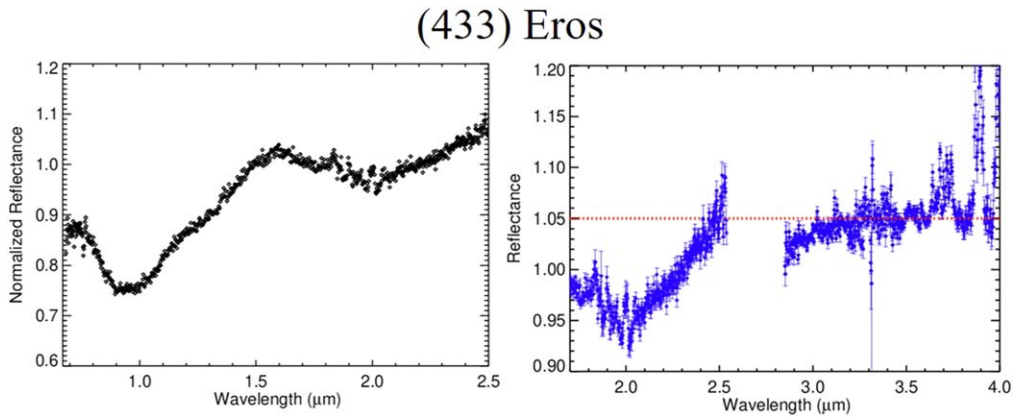

Figure A1. Spectra of the S-Complex NEA (433) Eros as observed on 2019 January 4 with a measured band depth of 2.5% ± 1.1%. The prism spectrum is on the left; the LXD_short spectrum is on the right. The red dashed line represents the reflected continuum.

(The complete figure set (32 images) is available.)

ORCID iDs

J. P. Emery https://orcid.org/0000-0001-9265-9475
C. A. Thomas https://orcid.org/0000-0003-3091-5757
A. R. Rivkin https://orcid.org/0000-0002-9939-9976

References

Aznar, A., de Leon, J., Popescu, M., et al. 2019, MNRAS, 483, 4820
Benedict, W. S., & Plyler, E. K. 1951, JRNBS, 46, 246
Binzel, R. P., DeMeo, F. E., Turtelboom, E. V., et al. 2019, Icar, 324, 41
Binzel, R. P., Reddy, V., & Dunn, T. 2015, in Asteroids IV, ed. P. Michel, F. E. DeMeo, & W. F. Bottke (Tucson, AZ: Univ. Arizona Press), 243
Bottke, W. F., Jr., Morbidelli, A., Jedicke, R., et al. 2002, Icar, 156, 399
Brearley, A. J., & Jones, R. H. 1998, in Planetary Materials, Vol. 36, ed. J. J. Papike (Chantilly, VA: Mineralogical Society of America), 3–001
Britt, D. T., Yeomans, D., Housen, K., & Consolmagno, G. 2002, in Asteroids III, ed. W. F. Bottke, Jr. (Tucson, AZ: Univ. Arizona Press), 485
Burbine, T. H., Buchanan, P. C., & Binzel, R. P. 2007, LPSC, 38, 2117
Burbine, T. H., Buchanan, P. C., Dolkar, T., & Binzel, R. P. 2009, M&PS, 44, 1331
Burke, D. J., Dukes, C. A., Kim, J.-H., et al. 2011, Icar, 211, 1082
Clark, R. N. 2009, Sci, 326, 562
Cushing, M. C., Vacca, W. D., & Rayner, J. T. 2004, PASP, 116, 362
De Sanctis, M. C., Ammannito, E., Capria, M. T., et al. 2013, M&PS, 48, 2166
De Sanctis, M. C., Ammannito, E., Carrolzzo, F. G., et al. 2018, M&PS, 53, 1844
De Sanctis, M. C., Combe, J. P., Ammannito, E., et al. 2012, ApJL, 758, L36
Delbo, M., Mueller, M., Emery, J. P., Rozitis, B., & Capria, M. T. 2015, in Asteroids IV, ed. P. Michel, F. E. DeMeo, & W. F. Bottke (Tucson, AZ: Univ. Arizona Press), 107
DeMeo, F. E., Alexander, C. M. O'D., Walsh, K. J., Chapman, C. R., & Binzel, R. P. 2015, in Asteroids IV, ed. P. Michel, F. E. DeMeo, W. F. Bottke et al. (Tucson, AZ: Univ. Arizona Press), 13
DeMeo, F., & Binzel, R. P. 2008, Icar, 194, 439
DeMeo, F. E., Binzel, R. P., Slivan, S. M., & Bus, S. J. 2009, Icar, 202, 160
DeMeo, F. E., & Carry, B. 2013, Icar, 226, 723
Dunn, T. L., Burbine, T. H., Bottke, W. F., Jr., & Clark, J. P. 2013, Icar, 222, 273
Dunn, T. L., McCoy, T. J., Sunshine, J. M., & McSween, H. Y., Jr. 2010, Icar, 208, 789
Farrell, W. M., Hurley, D. M., Esposito, V. J., McLain, J. L., & Zimmerman, M. I. 2017, JGRE, 122, 269
Farrell, W. M., Hurley, D. M., & Zimmerman, M. I. 2015, Icar, 255, 116
Frere, N. 2021, PhD thesis, Univ. Tennessee, https://trace.tennessee.edu/utk_gradthes/6217/
Gaffey, M. J., Bell, J. F., Brown, R. H., et al. 1993, Icar, 106, 573
Greenwood, J. P., Itoh, S., Sakamoto, N., et al. 2011, NatGe, 4, 79
Grossman, L., & Larimer, J. W. 1974, RvGeo, 12, 71
Grün, E., & Zook, H. A. 1980, in Dynamics of Micrometeoroids, Symposium–International Astronomical Union, Vol. 90 (Cambridge: Cambridge Univ. Press), 293
Gundlach, B., & Blum, J. 2013, Icar, 223, 479
Hanuš, J., Delbo, M., Ďurech, J., & Alí-Lagoa, V. 2015, Icar, 256, 101
Hapke, B. 2001, JGR, 106, 10,039
Harris, A. W. 1998, Icar, 131, 291
Hasegawa, S., Murakawa, K., Ishiguro, M., et al. 2003, GeoRL, 30, 2123
Hinkle, M. L., Howell, E. S., Fernández, Y. R., et al. 2022, Icar, 382, 114939
Honniball, C. I., Lucey, P. G., Li, S., et al. 2021, NatAs, 5, 121
Ieva, S., Dotto, E., Lazzaro, D., et al. 2015, MNRAS, 455, 2871
Landsman, Z. A., Campins, H., Pinilla-Alonso, N., Hanus, J., & Lorenzi, V. 2015, Icar, 252, 186
Lebofsky, L. A. 1980, AJ, 85, 573
Lebofsky, L. A., & Spencer, J. R. 1989, in Asteroids II, ed. R. P. Binzel, T. Gehrels, & M. S. Matthews (Tucson, AZ: Univ. Arizona Press), 128
Lee, P. 1996, Icar, 124, 181
Leith, T. B., Moskovitz, N. A., Mayne, R. G., et al. 2017, Icar, 295, 61
Lewis, J. S., & Huston, M. L. 1993, in Resources of Near-Earth Space, ed. Lewis, Matthews, & Guerrieri (Tucson, AZ: Univ. Arizona Press), 523
Lindsay, S. S., Dunn, T. L., Emery, J. P., & Bowles, N. E. 2016, M&PS, 51, 806
Lindsay, S. S., Marchis, F., Emery, J. P., Enriquez, J. E., & Assafin, M. 2015, Icar, 247, 53
Lucas, M. P., Emery, J. P., Hiroi, T., & McSween, H. Y. 2018, M&PS, 54, 157
Lunine, I. J. 2006, in Meteorites and the Early Solar System II, ed. D. S. Lauretta & H. Y. McSween, Jr. (Tucson, AZ: Univ. Arizona Press), 309
MacLennan, E. 2019, PhD dissertation, Univ. Tennessee, https://trace.tennessee.edu/utk_graddiss/5467
Mainzer, A., Bauer, J., Cutri, R., et al. 2019, NEOWISE Diameters and Albedos V2.0, urn:nasa:pds:neowise_diameters_albedos::2.0., NASA Planetary Data System, doi:10.26033/18S3-2Z54
Mainzer, A. K., Bauer, J. M., Cutri, R. M., et al. 2016, NEOWISE Diameters and Albedos V1.0. EAR-A-COMPIL-5-NEOWISEDIAM-V1.0, NASA Planetary Data System, https://sbnarchive.psi.edu/pds3/non_mission/EAR_A_COMPIL_5_NEOWISEDIAM_V1_0/
Marchi, S., Delbo, M., Morbidelli, A., Paolicchi, P., & Lazzarin, M. 2009, MNRAS, 400, 147
McCord, T. B., Li, J. Y., Combe, J. P., et al. 2012, Natur, 491, 83
McCord, T. B., Taylor, L. A., Combe, J.-P., et al. 2011, JGRE, 116, E00G05
Morbidelli, A., Chambers, J., Lunine, J. I., et al. 2000, M&PS, 35, 1309
Mueller, M. 2007, PhD thesis, Free Univ. of Berlin
Muralidharan, K., Deymier, P., Stimpfl, M., de Leeuw, N. H., & Drake, M. J. 2008, Icar, 198, 400
Neumann, G. A., Cavanaugh, J. F., Sun, X. L., et al. 2013, Sci, 339, 296
Nichols, C. R. 1993, in Resources of Near-Earth Space, ed. Lewis, Matthews, & Guerrieri (Tucson, AZ: Univ. Arizona Press), 543
Nicolaou, G., Livadiotis, G., Wicks, R. T., Verscharen, D., & Maruca, B. A. 2020, ApJ, 901, 26
Opeil, C. P., Consolmagno, G. J., Safarik, D. J., & Britt, D. T. 2012, M&PS, 47, 319
Orlando, T. M., Jones, B., Paty, C., et al. 2018, Chem, 4, 8
Perna, D., Barucci, M. A., & Fulchignoni, M. 2013, A&ARv, 21, 28
Pieters, C. M., Goswami, J. N., Clark, R. N., et al. 2009, Sci, 326, 568
Poch, O., Istiqomah, I., Quirico, E., et al. 2020, Sci, 367, eaaw7462
Pokorný, P., Mazarico, E., & Schorghofer, N. 2021, PSJ, 2, 85
Popescu, M., Birlan, M., Nedelcu, D. A., Vaubaillon, J., & Cristescu, C. P. 2014, A&A, 572, 16
Prettyman, T. H., Mittlefehldt, D. W., Yamashita, N., et al. 2012, Sci, 338, 242
Rayner, J. T., Toomey, D. W., Onaka, P. M., et al. 2003, PASP, 115, 362
Reddy, V., Dunn, T. L., Thomas, C. A., Moskovitz, N. A., & Burbine, T. H. 2015a, in Asteroids IV, ed. P. Michel, F. E. DeMeo, & W. F. Bottke (Tucson, AZ: Univ. Arizona Press), 43
Reddy, V., Gary, B. L., Sanchez, J. A., et al. 2015b, ApJ, 811, 65
Reddy, V., Kelley, M. S., Dotson, J., et al. 2022, Icar, 374, 114790
Reddy, V., Le Corre, L., O'Brien, D. P., et al. 2012a, Icar, 221, 544
Reddy, V., Sanchez, J. A., Nathues, A., et al. 2012b, Icar, 217, 153
Rivkin, A. S. 2010, BAAS, 42, 1073
Rivkin, A. S., & Emery, J. P. 2010, Natur, 64, 1322
Rivkin, A. S., Howell, E. S., Britt, D. T., et al. 1995, Icar, 117, 90
Rivkin, A. S., Howell, E. S., & Emery, J. P. 2019, JGRE, 124, 1393
Rivkin, A. S., Howell, E. S., Emery, J. P., & Sunshine, J. 2018, Icar, 304, 74
Rivkin, A. S., Howell, E. S., Lebofsky, L. A., Clark, B. E., & Britt, D. T. 2000, Icar, 145, 351
Rivkin, A. S., Howell, E. S., Vilas, F., & Lebofsky, L. A. 2002, in Asteroids III, ed. W. F. Bottke, Jr. et al. (Tucson, AZ: Univ. Arizona Press), 235
Ruiz, J. A., Gonzales, J., Tai Udovicic, C. J., & Edwards, C. S. 2020, AGUFM, P085-06
Sanchez, J. P., & McInnes, C. R. 2012, AcAau, 73, 49
Sanchez, J. A., Reddy, V., Nathues, A., et al. 2012, Icar, 220, 36
Sanchez, J. A., Reddy, V., Thirouin, A., et al. 2019, AJ Letters, 881, 6
Sanchez, J. A., Thomas, C. A., Reddy, V., et al. 2020, AJ, 159, 10
Schaible, M. J., & Baragiola, R. A. 2014, JGRE, 119, 2017
Simon, A. A., Donaldson Hanna, K. L., Drouet d'Aubigny, C. Y., et al. 2019, GeoRL, 46, 6322
Smith, A. G. 1967, in Radio Exploration of the Sun, ed. D. Van Nostrand (Princeton, NJ: Van Nostrand)
Springmann, A., Lauretta, D. S., Klaue, B., et al. 2019, Icar, 324, 104
Starukhina, L. 2001, JGR, 106, 14701
Starukhina, L. V. 2003, SoSyR, 37, 36
Starukhina, L. V. 2006, AdSpR, 37, 50
Sunshine, J. M., Farnham, T. L., Feaga, L. M., et al. 2009, Sci, 326, 565
Takir, D., & Emery, J. P. 2012, Icar, 219, 641
Takir, D., Kareta, T., Emery, J. P., et al. 2020, NatCo, 11, 2050
Takir, D., Reddy, V., Sanchez, J. A., Shepard, M. K., & Emery, J. P. 2017, AJ, 153, 31
Thomas, C. A., Emery, J. P., Trilling, D. E., et al. 2014, Icar, 228, 217
Vacca, W. D., Cushing, M. C., & Rayner, J. T. 2003, PASP, 115, 389
Valdes, F. 2019, arXiv:1901.07111
Vernazza, P., Mothé-Diniz, T., Barucci, M. A., et al. 2005, A&A, 436, 1113
Warner, B. D., Harris, A. W., & Pravec, P. 2009, Icar, 202, 134

Wigton, N. 2015, Master's thesis, Univ. Tennessee, Knoxville, https://trace.tennessee.edu/utk_gradthes/3457
Wöhler, C., Grumpe, A., Berezhnoy, A. A., & Shevchenko, V. V. 2017, SciA, 3, e1701286
Yamada, M., Sasaki, S., Nagahara, H., et al. 1999, EP&S, 51, 1255
Yeomans, D. K., Antreasian, P. G., Barriot, J.-P., et al. 2000, Sci, 289, 2085
Zellner, E. J., Ronca, L. B., & Levy, P. W. 1966, JGR, 71, 4855
Zhu, C., Crandall, P. B., Gillis-Davis, J. J., et al. 2019, PNAS, 116, 11165